Università degli Studi di Trieste

DIPARTIMENTO DI FISICA
Corso di Laurea Magistrale in Fisica
Curriculum in Microfisica e Fisica della Materia

Studio della dinamica delle quasi-particelle eccitate alla superficie di materiali Rashba di volume

A glance on hot quasiparticles dynamics at the surface of bulk Rashba materials

Candidato:
Marta Zonno
Matricola SM2300095

Relatore:
Prof. Fulvio Parmigiani

Correlatore:
Dott. Alberto Crepaldi

Anno Accademico 2012-2013

To my family,

who always believed in me

Sommario

In questi ultimi anni la spintronica ha attratto grande interesse e diversi studi sono stati indirizzati alla comprensione delle properietà elettriche e magnetiche di materiali con caratteristiche particolari di spin al livello di Fermi. In particolare, la creazione e la manipolazione di correnti di spin richiedono che l'energia tra i due canali di spin sia maggiore di k_BT. Inoltre, un grande *spin splitting* riduce la lunghezza di coerenza del campo di spin necessaria per orientare la corrente di spin sotto l'azione di un campo magnetico esterno.

Recentemente la ricerca di questi materiali si è focalizzata sugli isolanti topologici e sui sistemi Rashba, in cui la degenarazione di spin, dovuta ad un forte accoppiamento *spin-orbit*, risulta rotta a causa della perdita di simmetria spaziale nel solido. In questo contesto, lo studio delle proprietà elettroniche e di spin in questi materiali, come lo studio dell'accoppiamento elettrone-fonone che determina gli eventi di scattering che limitano le proprietà di trasporto di tali materiali, acquista un'importanza fondamentale.

Questa tesi è quindi finalizzata allo studio dello scattering elettrone-fonone, attraverso spettroscopie fotoelettroniche fuori equilibrio, nei semiconduttori BiTeX (con X = I, Cl, Br) che rappresentano il primo esempio di materiali tridimensionali caratterizati da un grande Rashba *spin splitting* di volume.

In particolare, si è studiata la struttura elettronica dipendente dal tempo degli stati *spin-split* in BiTeI utilizzando la spettroscopia di fotoemissione risolta in angolo e in tempo (tr-ARPES). Tale tecnica combina ARPES convenzionale con impulsi laser ultracorti e permette l'indagine delle proprietà elettroniche fuori equilibrio. Infatti, misurando l'evoluzione temporale della densità delle particelle eccitate negli stati di superficie *spin-split*, siamo stati in grado di studiare i principali parametri dinamici, comunemente definiti come la temperatura elettronica efficace T^*_{el} e il potenziale chimico efficace μ^*. Dall' evoluzione temporale di T^*_{el} abbiamo stimato, utilizzando uno specifico set di equazioni, la constante che descrive l'accoppiamento elettrone-fonone λ. Infine, analizzando la dinamica della funzione spettrale di singola particella, sono state ottenute informazioni sui meccanismi di scattering microscopico.

Per completare i nostri studi abbiamo analizzato il dicroismo che caratterizza

gli stati di superficie *spin-split* della famiglia di semiconduttori BiTeX, utilizzando l'ARPES in dicroismo circolare (CD-ARPES). Il segnale dicroico, che viene ottenuto attraverso la differenza dell'intensità di fotoemissione ottenuta con le due opposte elicità dei fotoni incidenti, è stato recentemente proposto come una misura diretta dello spin e del momento orbitale angolare in sistemi con un forte accoppiamento *spin-orbit*. Attraverso questa tesi mostriamo con chiara evidenza sperimentale come gli effetti dicroici nei materiali BiTeX siano in funzione dell'energia dei fotoni incidenti, aprendo domande fondamentali sull'origine di tale dicroismo che sembra compromettere la spiegazione fornita dagli attuali modelli di fotoemissione in dicroismo. Certamente, i risultati che riportiamo saranno oggetto di ulteriori studi volti a comprendere in maniera completa ed esaustiva la fisica del dicroismo osservato attraverso la fotoemissione a basse energie.

La tesi è organizzata nel modo seguente: dopo l'introduzione fornita nel Capitolo 1, il Capitolo 2 presenta i modelli teorici che descrivono la rottura della degenerazione di spin in assenza di simmetria di inversione spaziale e i primi studi ARPES compiuti sulla famiglia BiTeX (con X = I, Cl, Br). Il Capitolo 3 descrive la tecnica ARPES all'equilibrio e fuori equilibrio e il *setup* ottico sperimentale. Il Capitolo 4 presenta le misure tr-ARPES effettuate al laboratorio T-ReX su BiTeI, l'analisi della distribuzione di Fermi-Dirac e della funzione spettrale di singola particella, e il calcolo della costante di accoppiamento elettrone-fonone λ. Il Capitolo 5 riporta le misure CD-ARPES sulla famiglia estesa BiTeX, con particolare attenzione all'analisi del segnale dicroico in funzione dell'energia dei fotoni incidenti. Infine, il Capitolo 6 riassume i principali risultati e conclusioni articolati nei capitolo precedenti.

Contents

1 Introduction **1**

2 Spin degeneracy lifting at the surface and in the bulk of solids **3**
2.1 Spin-split surface states: the Rasbha-Bychkov model 4
2.2 Non-centrosymmetric bulk materials 6
2.3 Giant Rashba spin splitting in bulk BiTeI 7
2.3.1 The discovery of large spin splitting in bulk BiTeI 8
2.4 Bulk spin-split states in BiTeX 11

3 Equilibrium and Non-equilibrium ARPES **15**
3.1 Introduction to Angle Resolved PhotoEmission Spectroscopy . . 15
3.2 Conservation of the energy and the momentum in ARPES 18
3.3 Intensity of photoemission 19
3.3.1 The matrix element 22
3.4 Time-resolved ARPES 24
3.4.1 Pump-Probe technique 25
3.4.2 Laser system 25
3.4.3 Pump-Probe setup 26
3.4.4 Characterization of the probe pulse 27

4 Time-resolved ARPES measurements on BiTeI **31**
4.1 Measurement conditions 31
4.2 Equilibrium and non-equilibrium electronic properties of spin-split states of BiTeI 32
4.3 EDCs analysis of the density of states 34
4.3.1 Evolution of the effective electronic temperature T_{el}^{*} . . . 37
4.3.2 Evolution of the effective chemical potential μ^{*} 42
4.4 MDCs analysis 44
4.5 Electron-Phonon coupling in the spin-split states of BiTeI 48
4.5.1 The Two Temperatures Model 49
4.5.2 The Two Temperatures Model on BiTeI 50

4.5.2.1 Modelling the absorbed power density 51
4.5.2.2 Electron-Phonon coupling constant in BiTeI . . 54

5 Dichroic ARPES on BiTeX **57**
5.1 Physical interpretation of the CD-ARPES in strong spin-orbit coupled systems 57
5.2 Circular dichroic ARPES measurements on BiTeX 62
5.2.1 Measurement conditions 62
5.2.2 Dichroic constant energy mapping of BiTeI 63
5.2.3 Energy evolution of dichroism in BiTeX 64
5.3 Discussion and future investigations 69

6 Conclusions **71**

Bibliography **73**

Ringraziamenti **79**

Chapter 1

Introduction

In these last years spintronics has attracted large interest and several studies have been focused on the understanding of the electronic and magnetic properties of materials displaying a non trivial spin texture at the Fermi level. In particular, the creation and manipulation of spin currents require materials where the energy separation between the spin channels larger than k_BT. Furthermore, a large spin splitting reduces the spin-field coherence length requested to orient the spin current under the effect of an external magnetic field.

The search for these materials has been recently focused on topological insulators and systems where the spin degeneracy, due to a strong spin-orbit interaction, is lifted by the lack spatial symmetry, i.e. Rashba systems. In this perspective, the investigation of the spin and electronic properties in these materials is of paramount importance , as well as the study of the electron-phonon coupling , that determines scattering events which limit the transport properties of these materials.

This thesis is aimed to study the electron-phonon scattering by non-equilibrium photoelectron spectroscopies in layered semiconductors BiTeX (with X= I, Cl and Br), being these the first example of three-dimensional materials characterized by a bulk giant Rashba spin splitting.

In particular we studied the time-dependent electronic structure of the spin-split states in BiTeI through time-resolved and angle resolved photoemission spectroscopy (tr-ARPES). This technique, by combining conventional ARPES with ultra-short laser pulses, allows investigating the electronic properties out of equilibrium. By detecting the temporal evolution of the density of the excited particles relevant to the spin-split surface states, we have been able to observe the main dynamical parameters usually defined as effective electronic temperature T^*_{el} and effective chemical potential μ^*. From the temporal evolution of T^*_{el} we estimated the electron-phonon coupling constant λ by using proper set of rate equations. Finally, by analyzing the dynamics of the one-particle spectral function information on the microscopic scattering mechanism has been

obtained.

Furthermore, to complement our non-equlibrium studies we have also investigated the dichroism characterizing the spin-split surface states of the semiconductor family BiTeX, by exploiting circular dichroic ARPES (CD-ARPES). The dichroic signal results as the difference between the photoemission intensities obtained with the two opposite helicities of the incoming photons and it has been recently proposed as a direct probe of the spin and orbital-angular momentum of strong spin-orbit coupled materials. Here we bring a clear experimental evidence of dichroic effects in BiTeX systems as a function of the energy of the incoming photons, therefore opening some fundamental questions about its origin that seems to overtake the actual dichroic photoemission understanding and models. Of course, these findings will be matter of further studies in order to fully describe the physics of the PES dichroisms at low photon energies.

The thesis is organized as follow: after the introduction of Chapter 1, Chapter 2 presents the theoretical models describing the lifting of the spin degeneracy in the absence of spatial symmetry and the first ARPES studies performed on the BiTeX family (with $X=$ I, Cl and Br). Chapter 3 describes the equilibrium and non-equilibrium ARPES technique and the optical experimental setup. Chapter 4 presents the tr-ARPES measurements performed at the T-Rex laboratory on BiTeI, the analysis of the Fermi-Dirac distribution and the one-particle spectral function and the estimation of the electron-phonon coupling constant λ. Chapter 5 illustrates the CD-ARPES measurements on the extended family BiTeX, focusing on the analysis of the dichroic signal as a function of the photons energy. Finally, Chapter 6 summarizes the most important results and conclusions outlined in the previous chapters.

Chapter 2

Spin degeneracy lifting at the surface and in the bulk of solids

The advent of the forthcoming spintronics devices is based on the fascinating perspective to exploit the intrinsic electronic magnetic moment associated to the spin degree of freedom. In this context, the possibility to create and manipulate spin currents is given by the Rashba effect. This effect consists in the lifting of the spin degeneracy through the spin-orbit interaction in systems which lack spatial symmetry. This mechanism was described first by Rashba and Dresselhaus in bulk materials with wurtzite [1] and zinc-blend [2] crystal structure. Recently, Rashba and Bychkov have shown that any surface offers the possibility to resolve the spin degeneracy of a confined two-dimensional electron gas [3].

The Dresselhaus spin splitting was experimentally reported by means of photocurrent and magnetoresistance measurements [4, 5] in quasi two-dimensional systems, such as the interfaces of semiconductor heterostructures. The magnitude of the spin splitting for Dresselhaus-like systems is small (< 1 meV) and far below the actual experimental resolution limits for techniques like angle resolved photo-electron spectroscopy (ARPES). Whereas, two-dimensional electron gases at the surface of various metals (Au(111) [6], Bi [7], W(110)[8], Ir(111)[9]) display a spin splitting large enough to be detected by ARPES.

After the direct observation of the Rashba-Bychkov spin splitting in a two-dimensional gas, the experimental challenge has become to directly report the giant splitting in the band structure of a three-dimensional system. Therefore, non-centrosymmetric materials with three-dimensional band structure have been investigated. An example of these compounds is represented by the layered semiconductor BiTeI (Bismuth-Tellurium-Iodine), in which the existence of spin-split states have been recently proposed by *ab initio* calculations and

and later confirmed by ARPES experiments.

This chapter illustrates the Rashba-Bychkov model providing a simple description of the spin splitting occurring in a two-dimensional electron gas, and the conditions necessary to originate a spin splitting in a non-centrosymmetric three-dimensional material. Finally, the discovery of the giant Rashba-type spin splitting in bulk BiTeI, followed by the the first ARPES studies performed on the extended family BiTeX, (whit X= I, Br and Cl), is reported.

2.1 Spin-split surface states: the Rasbha-Bychkov model

In solid state physics textbooks, the electronic density of states is assumed to have a double occupancy in the absence of a magnetic field [10, 11]. Each band is double occupied in order to accommodate the two spin components. In general, each degeneracy of the eigenstates results from a specific symmetry of the Hamiltonian describing the system. In our case, the spin degeneracy is a consequence of the inversion symmetry (I) and time reversal symmetry (TR) in the solid. If one of this two is broken, the spin-orbit (SO) coupling can split the bands of the two spin components.

The effects on the band structure of a material of the I and TR symmetries are mathematically described as,

$$\left.\begin{array}{rcl} \text{I} & \rightarrow & E_{(\mathbf{k},\uparrow)} = E_{(-\mathbf{k},\uparrow)} \\ \text{TR} & \rightarrow & E_{(\mathbf{k},\uparrow)} = E_{(-\mathbf{k},\downarrow)} \end{array}\right\} \quad E_{(\mathbf{k},\uparrow)} = E_{(-\mathbf{k},\downarrow)} = E_{(\mathbf{k},\downarrow)} = E_{(-\mathbf{k},\uparrow)} \qquad (2.1)$$

In equation 2.1, both the symmetry operations change the wave vector $\mathbf{k}$ into $-\mathbf{k}$, however TR also flips the spin. Therefore, the combination of the two effects results in the twofold degeneracy of the eigenvalues. In the presence of the space inversion asymmetry, the spin degenerate levels can be split into two different states having opposite spin if the SO coupling is not zero.

Interestingly, the lack of I always occurs at the surface of solids, where the periodicity along the direction normal to the surface is broken. The Rashba-Bychkov model describes the SO interaction of a two-dimensional electron gas confined at the surface [3]. By adopting a relativistic description, an electron moving at the surface with velocity $\mathbf{v}$, under the effect of an electric field $\mathbf{E}$, experiences an effective magnetic field $\mathbf{B}$ equal to $\mathbf{B} = \frac{\mathbf{v}\times\mathbf{E}}{c^2}$. In this description, the Hamiltonian obtained by including the SO interaction is,

$$H = \frac{|\mathbf{p}|^2}{2m} + V(x) + \frac{\hbar}{4m^2c^2}(\nabla V \times \mathbf{p}) \cdot \sigma \qquad (2.2)$$

where V is the surface electrostatic potential and σ are the Pauli matrices [12].

The electrons travelling at the surface are subject to a potential gradient $\nabla V = \frac{dV}{dz}\hat{e}_z$ where $\hat{e}_z$ represents the unitary vector orthogonal to the sample

surface. In this case, the perturbative Hamiltonian describing the spin-orbit interaction becomes the *Rashba-Bychkov Hamiltonian* [3]:

$$H_{SO} = \alpha_R(\sigma \times \mathbf{k}) \cdot \hat{e}_z \tag{2.3}$$

where α_R represents the Rashba parameter proportional to the surface potential gradient and it is the measure of the strength of the Rashba effect.

In the case of a parabolic band dispersion, the H_{SO} splits the parabolic dispersion of the nearly free electron gas in two different parabolic branches characterized by a **k**-linear splitting, as it is evident by solving the eigenvalue problem [12]:

$$H = \frac{\hbar^2\mathbf{k}^2}{2m} + \alpha_R(\sigma \times \mathbf{k}) \cdot \hat{e}_z \tag{2.4}$$

$$E^{\pm}(k_{\parallel}) = \frac{(k_{\parallel})^2}{2m} \pm \alpha_R k_{\parallel} \tag{2.5}$$

Figure 2.1 illustrates the calculated band dispersion associated to equation 2.5. A cut along k_x shows two parabolas shifted by the same quantity with respect to the $\overline{\Gamma}$ high symmetry point, where the spin degeneracy is maintained. Experimentally, a similar observation of a two $\mathbf{k}-$split parabolas was reported by LaShell et *al.* in an ARPES experiment investigating the surface states of Au(111) [6]. At a qualitative level, the experimentally resolved split surface states are well interpreted in term of the Rashba-Bychkov model. Unfortunately, from a quantitative point of view, the Rashba-Bychkov model provides a value for the energy splitting that is 4 orders of magnitude smaller than the experimental data (10^{-3} meV against the 2 meV measured at the Fermi level) [13]. For example, in spite of the important role played by the surface potential gradient, it cannot alone accounts for the magnitude of the Au(111) surface states splitting. In particular, recent studies proposed that the gradient potential involved in the Rashba-Bychkov model cannot be identified simply with the surface potential gradient, but the model must be generalized adequately to consider other different terms as for example the atomic spin-orbit coupling [14, 15, 16].

The important role played by the atomic spin-orbit coupling in defining the magnitude of the spin splitting was experimentally demonstrated by Reinert *et al.*. They compared, by means of ARPES, the electronic band structure of the various noble metal L-gap surface states, and they found that only Au(111) displayed a large and measurable spin splitting [17]. Only very recently, with the advent of ARPES with ultrahigh resolution, also the spin splitting of the Cu(111) surface states was resolved [18]. This suggests that the Rashba parameter α_R should take into account also the atomic spin-orbit coupling, which phenomenologically scales with the atomic number Z.

Petersen and Hedegård developed a tight-binding model to describe the Au(111) spin-split surface states [14]. In particular, in this model α_R is proportional to the atomic SO coupling through a parameter γ describing the asymmetry of the wavefunction. This wavefunction's asymmetry is introduced by the hopping integral between the in-plane p_{xy}-states and the out-of-plane p_z-component, which is possible in the presence of the surface potential $V(z)$.

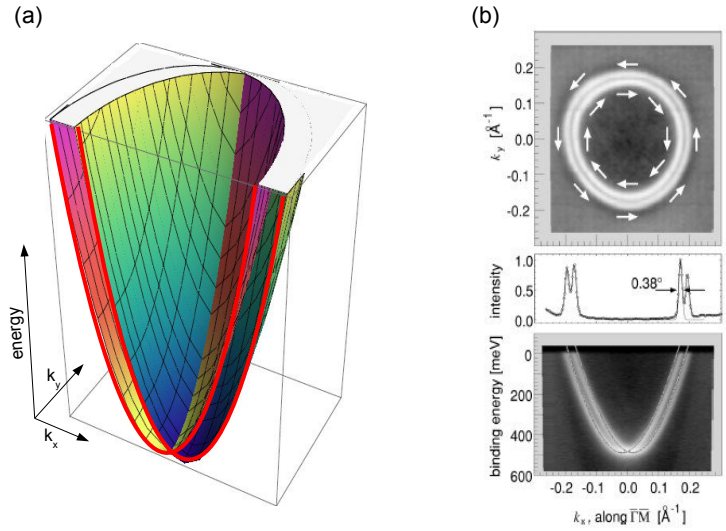


Figure 2.1: (a) calculated band structure of a 2D free-electron gas according to the Rashba-Bychkov model, with a cut along $k_y = 0$ that clearly displays two parabolas shifted by $\pm k_0$ (red lines); (b) 2D ARPES image of the Au(111) L-gap surface states. The upper panel shows the Fermi surface and the bottom panel illustrates the electronic dispersion. In both pictures the spin splitting is well resolved [13].

The resulting splitting is the consequence of the interplay between the surface potential gradient and the asymmetry of the surface states wavefunction, which also includes the information on the p-states atomic SO coupling.

2.2 Non-centrosymmetric bulk materials

In general, inversion symmetry is naturally broken at the surface of any solid. Whereas, in the bulk this is achieved only for crystals whose space group lacks inversion symmetry. As a result, the SO coupling can split also the bulk bands, with the exception of particular high symmetry points where the spin degeneracy is maintained [19]. The wurtzite and the zinc-blend are examples of non-centrosymmetric crystal structures, where the lifting of the spin degeneracy has been theoretically studied. In the former case the spin splitting are defined Rashba-type [1], while in the latter case are Dresselhaus-type [2].

After the discovery of a large Rashba-Bychkov spin splitting in two-dimensional surface states, the challenge was to resolve a giant splitting also in three-dimensional bulk systems.

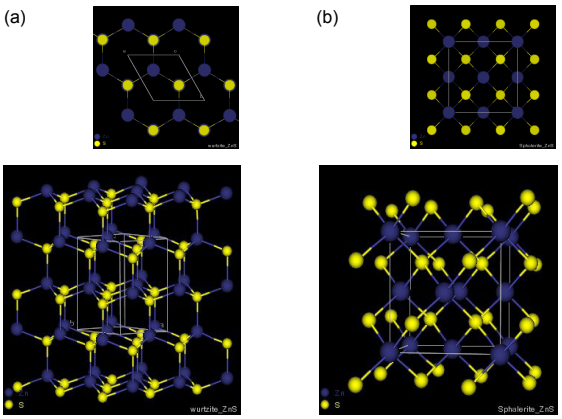


Figure 2.2: Non-centrosymmetric crystal structures: (a) wurtzite crystal structure having an hexagonal crystal packing; (b) zinc blend crystal structure consisting of two interpenetrating face centered cubic lattices displaced on quarter of a body diagonal. [20]

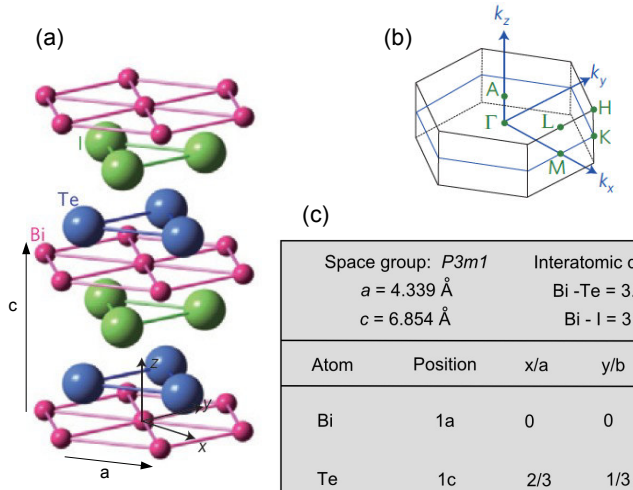
Baharamy and coworkers proposed three conditions necessary to obtain a giant Rashba-type splitting in bulk materials, in particular when dealing with bulk semiconductors, by developing the general $\mathbf{k} \cdot \mathbf{p}$ Hamiltonian in perturbation theory up to the second order [21]. The first requirement (i) is clearly the presence of large atomic SO interaction, due for example to the presence of large Z atoms, in non-centrosymmetric solid. The other two conditions are more difficult to be achieved and they are related to (ii) the narrowness of the band gap and to (iii) the parity of both the upper states of the valence band and the bottom states of the conduction band. The main conclusion of their work is that only states close in energy and with the same parity can effectively couple to each other resulting in a large spin splitting.

The non-centrosymmetric layered semiconductor BiTeI is an example of material that satisfies all the aforementioned conditions and recently, high resolution ARPES experiments, namely with spin resolution, have reported the presence of bulk spin-split bands, whose study is the subject of the next paragraphes.

2.3 Giant Rashba spin splitting in bulk BiTeI

BiTeI (Bismuth-Tellurium-Iodine) is a layered polar semiconductor that crystallizes in a hexagonal structure having a $P3m1$ space group and lattice constants $a = 4.339\,\text{Å}$ and $c = 6.854\,\text{Å}$. As shown in Figure 2.3, the crystal structure is characterized by the stacking of Bi, Te and I layers, with the bismuth atoms occupying the octahedral interstice sites. The BiTeI crystal structure, exhibiting

a smaller Bi-Te bond's length (Bi-Te = 3.039 Å) and a longer Bi-I bond's length (Bi-I = 3.272 Å), can be interpreted in terms of the semi-ionic model where the covalent coupling between Bi and Te atoms creates a positively charged bilayers $(BiTe)^{+}$, which interacts ionically with the I^{-} layer. Finally, there is a weaker Van der Waals bond between the Te and I layers. Interestingly, owing to the non-centrosimmetry of the material, the unique cleaving plane may result in two distinct cleave terminations (Te or I).



(c)

Space group: *P3m1*		Interatomic distances:		
a = 4.339 Å		Bi -Te = 3.039 Å		
c = 6.854 Å		Bi - I = 3.272 Å		
Atom	Position	x/a	y/b	z/c
Bi	1a	0	0	0
Te	1c	2/3	1/3	0.6928
I	1b	1/3	2/3	0.2510

Figure 2.3: (a) schematic representation of the BiTeI crystal structure [22]; (b) three-dimensional Brillouin zone with the high-symmetry points [22]; (c) table reporting the most important parameters of the BiTeI crystal structure, as obtained by X-ray powder diffraction study [23].

2.3.1 The discovery of large spin splitting in bulk BiTeI

The giant Rashba-type spin splitting in bulk BiTeI was reported first by Ishizaka and *al.*, by comparing spin resolved ARPES measurements with *ab initio* calculations [22]. The energy-band dispersion, obtained by using fully relativistic first-principles calculations, is shown in Figure 2.4 (a). The calculations help in assessing the orbital contributions to the various states. As a result, the conduction band above the Fermi level is mainly composed by the Bi 6*p* levels, whereas the valence band is mostly derived by Te and I 5*p* levels. Along the $\overline{\Gamma A}$ direction the spin degeneracy is preserved. However, for $k_{\parallel} \neq 0$ the valence and conduction bands in proximity of the Fermi level experience a large spin splitting. Such splitting is consistent of Baharamy et *al.* model [21]. BiTeI, in fact, displays a strong atomic SO interaction (due to the presence of bismuth

atoms) and it has a small energy band gap ($\sim 0.38\,\mathrm{eV}$). Finally the lower state of the conduction band and the upper state of the valence band at the point $\overline{A}$ have the same parity.

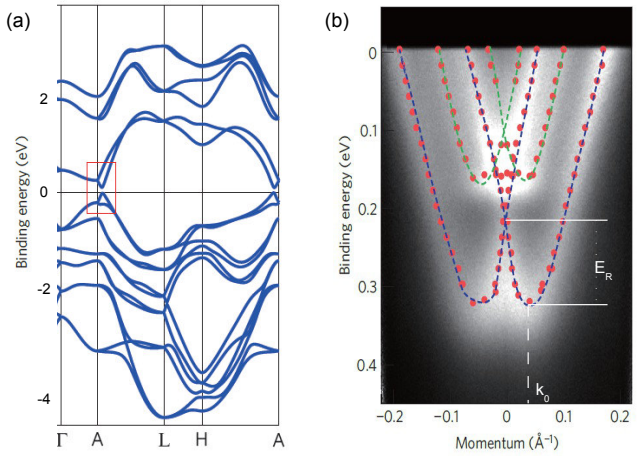


Figure 2.4: (a) energy-band dispersion obtained by relativistic first principle calculations [22]. The valence band minimum and the conduction band minimum appear slightly off the $\overline{A}$ high symmetry point ($k_{\|} = 0$ and $k_z = \pi/c$). Along the $\overline{\Gamma A}$ direction the spin degeneracy is maintained, but for $k_{\|} \neq 0$ the band dispersions are subject to large spin splitting; (b) $h\nu = 6.994\,\mathrm{eV}$ laser based ARPES image along $\overline{\Gamma M}$ direction. Two different sets of spin-split states are clearly resolved. They are interpreted as quantized subbands of the bulk conduction band due to the surface band-bending [22].

Figure 2.4 (b) shows an ARPES image along the $\overline{\Gamma M}$ high symmetry direction, measured with laser light with $h\nu = 6.994\,\mathrm{eV}$. Two sets of split bands are clearly resolved and they are characterized by a momentum offset of approximately $k_0 \sim 0.052\,\mathrm{\AA}^{-1}$, a Rashba energy $E_R \sim 0.1\,\mathrm{eV}$ (defined equal to $E_{cross} - E_{minimum}$) and a Rashba parameter $\alpha_R = 3.5\,\mathrm{eV\ \AA}$, which is the largest even reported [22]. The two pairs of states have binding energies equal to 0.33 eV and 0.17 eV, respectively. These states are interpreted as quantized subbands of the conduction band, resembling the subband structures observed in a quantum-well systems. For BiTeI, this quantization stems from the confinement of the conduction band electrons in the surface band-bending layer, a well known effect in semiconductor physics [24]. Therefore, the resulting subbands are confined to the topmost layers of the solid and they display two-dimensional character.

The different spin polarization of these bands was confirmed by spin resolved ARPES. Moreover, the good agreement between the experimental data and the theory is supporting the interpretation that the spin splitting of these two-dimensional states reflects the Rashba-type splitting of the bulk conduc-

tion band. Such idea is also supported by the fact that the contribution of the Rashba-Bytchkov-like surface spin splitting cannot alone explain the large values of $E_R \sim 0.1\,\text{eV}$ and $\alpha_R = 3.5\,\text{eV Å}$ [22].

In their recent work, Crepaldi and *al.* proposed an alternative interpretation for the origin of the two-dimensional spin-split states [25]. Among the two sets of states, one is attributed to the non-quantized bulk conduction band and the second is attributed to a surface derived state. Figure 2.5 reports the measured (a) and the calculated (b) band structure. In the latter the surface contribution, obtained by slab calculations, is shown with red lines, over-imposed to the bulk band structure, in blue. As explained in their work, the positively charged accumulation layer, due to the Te^+ termination, causes an effective downward shift of the conduction band. As a result, the Fermi level lies inside the conduction band, making it observable by ARPES. First-principles calculations show that the spin-split surface states coexiste with the bulk conduction band, which also exhibits a large splitting, with a slightly smaller momentum offset. Further surface states can be identified within the projected bulk gaps in the valence bands and they are characterized by a larger splitting than one already reported [22].

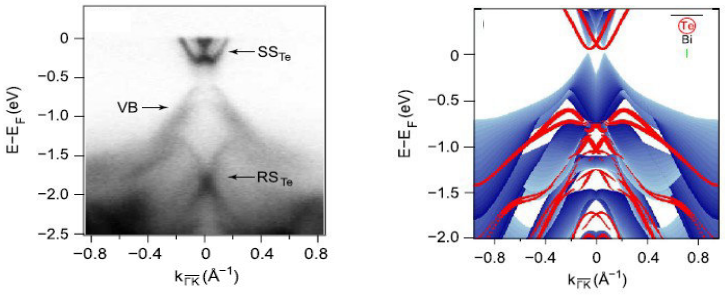


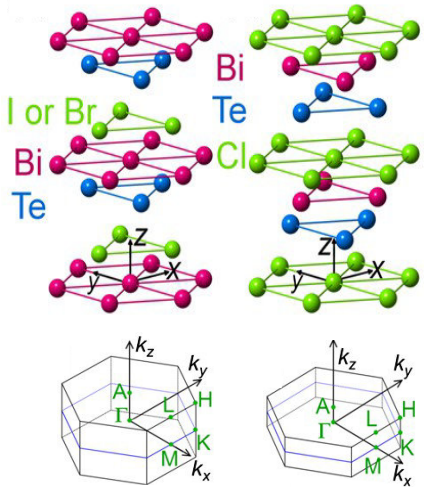
Figure 2.5: ARPES image along $\overline{\Gamma K}$ measured at 93 eV and $T = 40\,\text{K}$ as well as the corresponding firts-principles band structure calculations. The red lines represent the surface states, whereas the continuum of the bulk states is shown in blue [25].

We stress the fact that the fundamental property of these spin-split states is to be localized in the top-most surface layers, where the downward band bending takes place due to the charge accumulation at the surface. Furthermore, the insensitivity of the momentum offset k_0 to the manipulation of the surface potential gradient by means of alkali metal deposition, as reported by Crepaldi and *al.* [25], strongly supports that the large atomic SO coupling is mainly responsible for the magnitude of this large Rashba-like splitting.

2.4 Bulk spin-split states in BiTeX

The discovery of a giant Rashba-type spin splitting in both the surface and the bulk states of BiTeI, motivated similar investigations of the electronic band structure of the whole family of semiconductors BiTeX (with X= I, Br and Cl) [26].

(a)



(b)

	Compounds		
	BiTeI	BiTeBr	BiTeCl
Space group	P3m1	P3m1	P63mc
a (Å)	4.339	4.266	4.242
c (Å)	6.854	6.487	12.397
Interatomic distance (Å)	Bi–Te 3.039 Bi–I 3.272	Bi–Te 3.054 Bi–Br 3.054	Bi–Te 3.015 Bi–Cl 3.015

Figure 2.6: (a) schematic representation of BiTeX (X= I, Br and Cl) crystal structures and corresponding Brillouin zone with the high-symmetry points [26]; (b) table showing the most important parameters of the BiTeX structure as obtained by X-ray powder diffraction study [23].

The crystal structures of BiTeX is illustrated in Figure 2.6 (a). All the compounds crystallize in a hexagonal system with an alternating stacking of Bi, Te and X layers: BiTeBr and BiTeI belong to the $P3m1$ space group, while the BiTeCl belongs to the $P6_3mc$ space group. While BiTeBr has the same crystal structure of BiTeI, with Te and Br atoms ordered in alternating layers, in BiTeCl the layers of Te and Cl alternate along the c direction designing a four-layered packing. This structure has a unit cell almost twice as big as the unit cell of BiTeI and BiTeBr. The common feature of the three compounds is the semi-ionic character of their crystal structure. Each system presents a positively charged bilayer, resulting from the covalent bonding of Bi and Te, which interacts with the negatively charged halogen layer.

The ARPES measurements presented in Figure 2.7 clearly show that BiTeBr and BiTeCl also exhibit a giant spin splitting of the two-dimensional electron gas in the accumulation layer near the surface. In the ARPES maps of these

compounds three pairs of spin-split states are well resolved and they are characterized by a momentum offset smaller than the one reported for BiTeI.

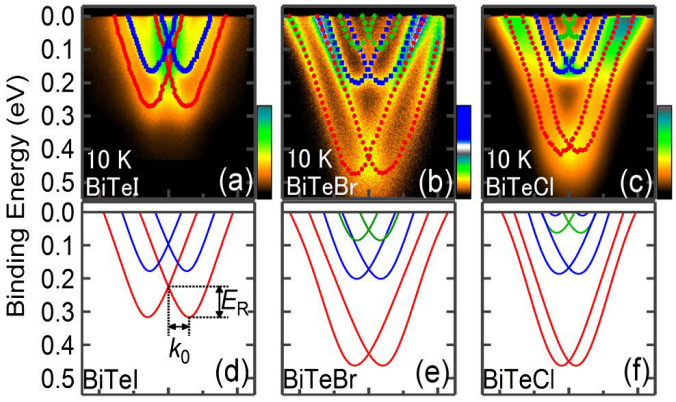


Figure 2.7: (a)-(c) ARPES maps of BiTeX (X= I, Br and Cl) obtained by using a laser source with $h\nu = 6.994\,\text{eV}$; (d)-(f) corresponding band dispersion calculations near the Fermi level. BiTeBr and BiTeCl exhibit three sets of Rashba spin-split states [26].

Table 2.1: Characteristic parameters quantifying the strength of the Rashba spin splitting in BiTeX (X= I, Br and Cl): Rashba energy E_R, momentum offset k_0, experimental and calculated Rashba parameters α_R and α_R^c. The index n indicates the set of states [26].

	BiTeI		BiTeBr			BiTeCl		
n	1	2	1	2	3	1	2	3
E_R (meV)	108	92	42	37	35	25	17	20
k_0 (10^{-3}Å^{-1})	50	47	43	38	34	26	20	18
α_R (eV Å)	4.3	3.9	2.0	2.0	2.1	1.9	1.7	2.2
α_R^c (eV Å)	3.06	3.02	1.78	1.67	1.84	1.28	1.29	1.78

Table 2.1 summarizes the most important parameters that characterize the Rashba-type spin-split states in BiTeX: E_R, k_0 and α_R. We focus on the Rashba strength parameter and we notice that its value is independent on the pair of spin-split states considered. Furthermore, α_R has a X dependence, in particular it decreases when passing from BiTeI to BiTeBr to BiTeCl. This behaviour can be explained by considering the band gap size in the three compounds, 0.36

eV, 0.6 eV and 0.7 eV respectively. As discussed in Section 2.1, the narrowness of the band gap is one of the fundamental conditions for realizing the giant Rashba-type splitting in a bulk system. Interestingly, the spin splitting in the BiTeX scales as the inverse of the band gap size.

Chapter 3

Equilibrium and Non-equilibrium ARPES

Photoemission Spectroscopy (PES) represents a powerful tool to investigate the electronic properties of solids. Among the PES techniques, the Angle Resolved Photoemission Spectroscopy (ARPES) can resolve both the energy and the momentum distribution of the photoemitted electrons, thus allowing the reconstruction of the electronic band structure of solid.

The first part of this chapter introduces the basic aspects of ARPES at equilibrium, primarily focusing on the kinematics and on the theoretical treatment of the photoemission intensity. In the second part the chapter illustrates the possibility to investigate the non-equilibrium electronic structure by time resolved ARPES (tr-ARPES). Finally, the pump-probe approach, the optical setup and the spectral and temporal characterization of the probe pulse are reported at the end of this chapter.

3.1 Introduction to Angle Resolved PhotoEmission Spectroscopy

The term PhotoEmission Spectroscopy (PES) refers to all "photon-in" $\longrightarrow$ "electron-out" techniques based on the linear photoelectric process. This effect was first experimentally discovered by Hertz in 1887, but only in 1905 Einstein developed a proper quantum based framework for interpret the PES data, meanwhile introducing the concept of photon.

When a monochromatic light of frequency ν illuminates the surface of a metal, an electron can absorb a photon. If the photon energy is larger than the metal work function, the electron can overtake the vacuum level reaching a free state with a kinetic energy equal to $E_{kin} = h\nu - \Phi - E_B$. E_B represents

the binding energy of the electron in the solid, while Φ represents the work function of the material, defined as the energy barrier that prevents the free electrons from escaping into the vacuum. Figure 3.1 shows a schematic of the photoemission process, where the sample (bottom left graph) is characterized by the valence band and two core levels, described by Dirac delta-like distributions. The corresponding photoelectron kinetic energy distribution (top right graph), produced after the adsorption of the incident photons with energy $h\nu$, is characterized by two gaussian peaks (due to the limited energy resolution of the technique) and one broad band.

In a PES experiment, the photoelectrons are collected by an electron energy analyser. Furthermore, several other degrees of freedom such as the energy, momentum and spin of the photoelectrons can be measured independently as a function of the energy and the polarization of the incident light, in the so-called angular-resolved and spin-resolved PES.

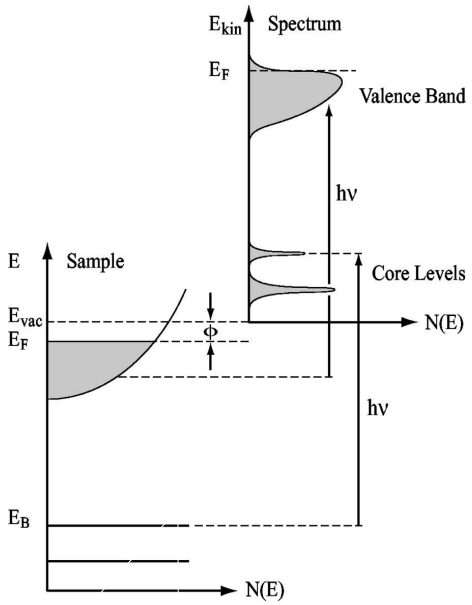


Figure 3.1: Photoelectric effect: relation between the energy levels in a metal and the electron kinetic energy distribution produced by incident photons with energy $h\nu$. The sample (bottom left graph) is characterized by the valence band and two core levels, while E_F, E_{vac}, Φ define the Fermi level, the vacuum level and the material work function respectively [27].

The electron mean free path, λ, is an important parameter to be considered when performing a photoemission experiment. It characterizes the average length travelled by a photoelectron inside the solid without undergoing any scat-

tering event (a so-called primary electron), and it determines the thickness of the sample from which the primary photoelectrons originate. Phenomenologically, λ is a function of the photon energy and this dependence is well shown by the "universal" curve of Figure 3.2. The adjective "universal" refers to the fact that, in spite of λ being related to the specific dielectric function of the material, the mean free paths measured in different materials but at the same photon energy are roughly equal. Figure 3.2 shows that the minimum of λ is found between 50 eV and 200 eV photon energy. Therefore, conventional tabletop UV light sources, such as He discharge lamp characterized by two emission lines at 21.22 eV and at 40.81 eV, produce a primary photoelectrons signal from the topmost atomic layers of the surface. More bulk sensitivity can be obtained by using X-ray sources such as Aluminium or Magnesium anodes ($AlK_\alpha \rightarrow 1486$ eV and $MgK_\alpha \rightarrow 1253$ eV).

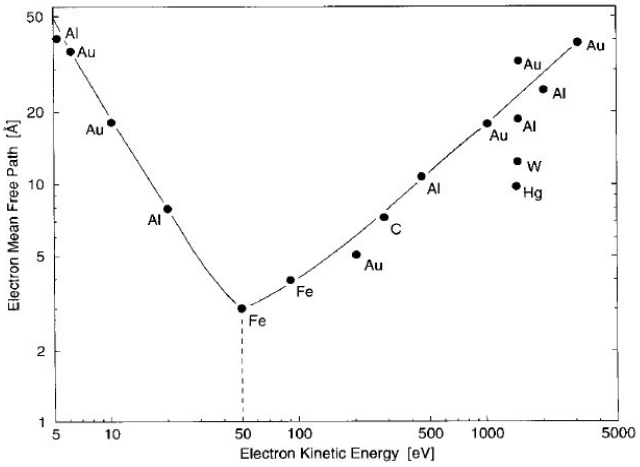


Figure 3.2: Universal curve characterizing the mean free path of photoelectrons in different materials. The minimum of the curve lies in the UV region (between 20 eV and 200 eV) [28].

PES experiments demand the use of Ultra High Vacuum (UHV) which is normally characterized by a pressure between 10^{-9} mbar and 10^{-11} mbar. The UHV is a necessary requirement in order to allow the maximum number of primary photoelectron to reach the detector and to prevent the absorption of contaminants at the sample surface.

In these last two decades ARPES has strongly developed after the advent of two-dimensional detectors able to determine in simultaneously the energy and momentum distributions of the electrons inside a material by measuring the photoelectrons intensity as a function of the kinetic energy at different emission

angles. Such measurement is typically achieved by hemispherical electron analyser (shown Figure 3.3), where the photoelectrons are deflected by the electric field created between the outer and inner hemispherical capacitor plates. The electron analyser is characterized by a plane of energy dispersion, whose angular acceptance is controlled by the width of the *entrance slit*. Some electrostatic lens are set between the sample and the entrance slit of the energy analyser in order to collect and retard/accelerate the photoelectrons before the entrance slit to match a special selected energy known as *Pass Energy*. This is the energy which characterizes the central circular trajectory inside the hemispherical capacitors. The angular dispersion of the electron analyser is thus controlled by these electrostatic lens (nowadays standard analyzer covers $\pm 10°$, whereas advanced analyser can cover up to $\pm 30°$). The two-dimensional detector set after the exit slit of the hemisphere allows the collection of ARPES images, where one axis is associated to the angular dispersion and the second is associated to the energy.

Figure 3.3 (b) shows an example of ARPES image: the photoemission intensity is reported as a function of energy (the y axis) and of the wave vector (the x axis) calculated from the angular dispersion through some mathematical relations that we explain in the next section.

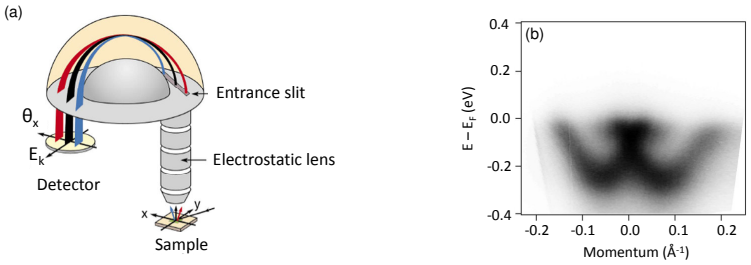


Figure 3.3: Angle-resolved photoemission spectroscopy: (a) electron spherical analyser with two-dimensional detector able to resolve simultaneously different kinetic energies and emission angles [27]; (b) ARPES image in which the x axis is associated to the wave vector and the y axis is associated to the binding energy.

3.2 Conservation of the energy and the momentum in ARPES

In order to reconstruct the information on the electronic initial states, it is necessary to connect the photoelectron energy and angular distributions measured outside the sample to the energy and the momentum distributions of the electrons inside the sample material.

Within the one-electron approximation, the energy conservation imposes the following condition among the binding energy E_B of the electronic states, the incident photon energy $h\nu$ and the kinetic energy E_{kin} of the photoelectron measured by the analyser [28]:

$$E_{kin} = h\nu - \Phi - |E_B| \tag{3.1}$$

The relation between the crystal momentum $\hbar\mathbf{k}$ of the electron inside the solid, and the momentum $\mathbf{p}$ of the photoelectron is more complex. In fact, since the surface breaks the solid translational symmetry, only $\mathbf{k}_{\parallel}$ is conserved. Whereas, the perpendicular component of the wave vector must be determined by measuring the surface barrier potential V_0. The modulus, as well as the parallel and perpendicular components of the photoelectron momentum are expressed by the following equations:

$$p = \sqrt{2mE_{kin}} \tag{3.2}$$

$$\mathbf{p}_{\parallel} = \hbar\mathbf{k}_{\parallel} = \sqrt{2mE_{kin}} \cdot (\hat{\mathbf{x}} \sin\theta \cos\Phi + \hat{\mathbf{y}} \sin\theta \sin\Phi) \tag{3.3}$$

$$p_{\perp} = \sqrt{2m(E_{kin} \cos^2\theta + V_0)} \tag{3.4}$$

where θ and Φ represent the polar and azimuthal angles, respectively.

Equations 3.1, 3.3 and 3.4 enable to determine completely the electronic band dispersion $E(\mathbf{k})$ of the solid starting from the photoelectrons kinetic energy and the polar and azimuthal emission angles distribution for a suitable ansatz of the surface potential V_0. Due to the difficulty in determining V_0, the ARPES technique is particularly suitable for the study of quasi-two-dimensional systems, in which the uncertainty in $k_{\perp}$ is negligible.

3.3 Intensity of photoemission

The creation and emission of a photoelectron is a more complex process than the one shown in Figure 3.1. In fact, in a very first approximation, the photoemission can only be viewed as a single particle process, whereas many-body interactions usually take place. A simplified model is given by *three-step process* (see in Figure 3.4), where each photoelectron undergoes three independent steps [28]: 1) the optical excitation induced by the absorption of the incident light; 2) the travelling of the excited electrons from the bulk towards the surface; 3) the penetration of the surface barrier potential by the electrons that escape into the vacuum as (almost) free particles. During the second step, the electrons can experience several inelastic scattering events through the solid, generating the so called secondary electrons signal, which constitutes a broad background that increases at low kinetic energies.

A formal semiclassical treatment of the photoemission process derives from the transition probability W_{if} calculated by the first order perturbation theory. Here, W_{if} describes an optical excitation between a N-electrons ground state,

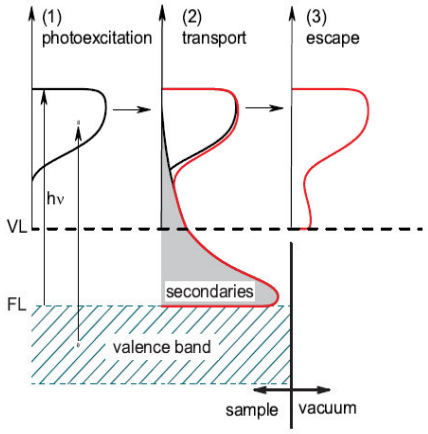


Figure 3.4: The three-step model description of the photoemission process: (1) optical excitation; (2) travel inside the solid; (3) escape into the vacuum. The shadow area corresponds to the secondaries electrons that undergo inelastic scattering processes. [28]

ψ_i^N, and one of the possible final states ψ_f^N:

$$W_{if} = \frac{2\pi}{\hbar}\left|\langle\psi_f^N|H_I|\psi_i^N\rangle\right|^2 \delta(E_f^N - E_i^N - h\nu) \tag{3.5}$$

where H_I represents the interaction with the incident photons and it is expressed as follow under the dipole approximation:

$$H_I = -\frac{e}{mc}(\mathbf{A}\cdot\mathbf{p}) \tag{3.6}$$

where $\mathbf{A}$ is the electromagnetic vector potential and $\mathbf{p}$ is the electronic momentum.

Some simplifications are needed in order to express the initial and final states of the system. The initial state is commonly defined as a single Slater-determinant-product between the one-electron function $\Phi_i^{\mathbf{k}}$ and the $(N-1)$-particle part:

$$\psi_i^N = \mathcal{A}\,\Phi_i^{\mathbf{k}}\psi_i^{N-1} \tag{3.7}$$

where $\mathcal{A}$ represents the operator that antisymmetrizes the Slater-determinant and it is necessary to satisfy the Pauli exclusion principle.

A further important approximation is introduced in the description of the final state, known as *sudden approximation*. Under this approximation a photoelectron is thought to be emitted without undergoing any interaction with the surrounding electrons and ions of the solid. The $(N-1)$-particle wavefunction

after sudden removal is not longer an eigenstate of the Hamiltonian and thus it can be expressed as a linear combination of the eigenfunctions ψ_m^{N-1}. The complete N-particle wavefunction is therefore expressed by:

$$\psi_f^N = \mathcal{A}\,\Phi_f^{\mathbf{k}} \sum_m \psi_m^{N-1} \tag{3.8}$$

The interaction Hamiltonian H_I (equation 3.6) affects only the one-electron function $\Phi^{\mathbf{k}}$, thus the matrix element in the equation 3.5 takes the following form:

$$\langle \psi_f^N | H_I | \psi_i^N \rangle = \langle \Phi_f^{\mathbf{k}} | H_I | \Phi_i^{\mathbf{k}} \rangle \langle \sum_m \psi_m^{N-1} | \psi_i^{N-1} \rangle = M_{if}^{\mathbf{k}} \langle \sum_m \psi_m^{N-1} | \psi_i^{N-1} \rangle \tag{3.9}$$

The total photoemission intensity, as a function of E_{kin} at the momentum $\mathbf{k}$, results proportional to:

$$I(E_{kin}, \mathbf{k}) \propto \sum_{if} |M_{if}^{\mathbf{k}}|^2 \sum_m \left| \langle \psi_m^{N-1} | \psi_i^{N-1} \rangle \right|^2 \delta(E_{kin} + E_m^{N-1} - E_i^N - h\nu) \tag{3.10}$$

where $E_f^N = E_{kin} + E_m^{N-1}$ is the final-state energy.

It follows that it is very convenient to introduce the formalism of second quantization theory in order to express the previous formula in terms of *one-particle spectral function*, which is defined as

$$A^-(\mathbf{k}, \omega) = \sum_m |\langle \psi_m^{N-1} | c_{\mathbf{k}}^- | \psi_i^N \rangle|^2 \delta(\hbar\omega + E_m^{N-1} - E_i^N) \tag{3.11}$$

where $c_{\mathbf{k}^-}$ is the operator of annihilation of an electron with momentum $\mathbf{k}$ and energy $\hbar\omega$. By using the spectral function, it is possible to express the photoemission intensity as:

$$I(E_{kin}, \hbar\omega) = I_0(\mathbf{k}, \nu, \mathbf{A}) A^-(\mathbf{k}, \omega) f(\hbar\omega) \tag{3.12}$$

where $f(\hbar\omega)$ corresponds to the Fermi-Dirac function describing the statistical distribution of the electrons in the system and $I_0(\mathbf{k}, \nu, \mathbf{A})$ is proportional to the modulus squared of the dipole transition matrix elements $M_{if}^{\mathbf{k}}$.

The spectral function $A(\mathbf{k}, \omega)$ is intimately connected to the one-particle Green's function $G(\mathbf{k}, E)$, representing a fundamental property of the N-electron system. It describes the probability that an electron in a state $\mathbf{k_1}$ is found in a state $\mathbf{k_2}$ if a scattering process with energy transfer E has occurred [28]. The analytic relation between $A(\mathbf{k}, E)$ and $G(\mathbf{k}, E)$ is expressed by the following:

$$G(\mathbf{k}, E) = \int_{-\infty}^{+\infty} \frac{A(\mathbf{k}, E')}{E - E' - i\delta} \tag{3.13}$$

$$A(\mathbf{k}, E) = \frac{1}{\pi} \mathcal{I}m\, G(\mathbf{k}, \mathbf{E}) \tag{3.14}$$

where δ is a positive infinitesimal and equation 3.14 is obtained from equation 3.13 by exploiting the identity $(E - E(\mathbf{k} - i\delta))^{-1} = \mathcal{P}[(E - E(\mathbf{k})^{-1})] + i\pi\delta(E - E(\mathbf{k}))$ which holds in the limit of $\delta \to 0^+$.

The fundamental advantage of describing the photoemission intensity in terms of the single-particle spectral function, is the possibility to extend easily the model when correlations are also considered. In particular the interaction between electrons and other particles can be included by introducing in the denominator of the Green function the complex *self-energy* $\Sigma(\mathbf{k}, \hbar\omega) = \Sigma^{'}(\mathbf{k}, \hbar\omega) + i\Sigma^{''}(\mathbf{k}, \hbar\omega)$. In this way, in the case of correlations, the one-electron Green's function, the spectral function and the photoemission intensity can be expressed as:

$$G(\mathbf{k}, \hbar\omega) = \frac{1}{\hbar\omega - \epsilon_{\mathbf{k}} - \Sigma^{'}(\mathbf{k}, \hbar\omega)} \tag{3.15}$$

$$A(\mathbf{k}, \hbar\omega) = -\frac{1}{\pi} \frac{\Sigma^{''}(\mathbf{k}, \hbar\omega)}{[\hbar\omega - \epsilon_{\mathbf{k}} - \Sigma^{'}(\mathbf{k}, \hbar\omega)]^2 + [\Sigma^{''}(\mathbf{k}, \hbar\omega)]^2} \tag{3.16}$$

$$I(\mathbf{k}, \hbar\omega) = -\frac{1}{\pi} I_0(\mathbf{k}, \nu, \mathbf{A}) f(\hbar\omega) \frac{\Sigma^{''}(\mathbf{k}, \hbar\omega)}{[\hbar\omega - \epsilon_{\mathbf{k}} - \Sigma^{'}(\mathbf{k}, \hbar\omega)]^2 + [\Sigma^{''}(\mathbf{k}, \hbar\omega)]^2} \tag{3.17}$$

where $\epsilon_{\mathbf{k}}$ is the electron's binding energy.

The real and imaginary part of electron self-energy contain all the information on the energy renormalization and lifetime of a quasiparticle propagating in the many-body correlated system.

3.3.1 The matrix element

The photoemission intensity is proportional to the square of the dipole matrix element, $M_{if}^{\mathbf{k}} = \langle \Phi_f^{\mathbf{k}} | H_I | \Phi_i^{\mathbf{k}} \rangle$, as discussed in the previous section. Therefore, it depends also on the experimental geometry, the polarization of the incident light and the photon energy.

The general form of the matrix element can be expressed as a function of the polarization vector of the incident photon, ϵ, by using the commutation rule $\hbar\mathbf{p}/m = -i[\mathbf{x}, H]$:

$$|M_{if}^{\mathbf{k}}|^2 \propto |\langle \Phi_f^{\mathbf{k}} | \epsilon \cdot \mathbf{A} | \Phi_i^{\mathbf{k}} \rangle|^2 \tag{3.18}$$

It is evident that equation 3.18 shows selection rules that depends on the parity of the operator and wavefunctions, as well as on the geometry of the photoemission process. Therefore, the matrix element can be equal to zero resulting in a complete suppression of the photoemission intensity. For instance, by considering photoemission from a $d_{x^2-y^2}$ orbital with the detector set in the mirror plane (Figure 3.5), the total integral must be even under reflection with respect to the mirror plane in order to have a non-vanishing photoemission signal [27]. Since the final state wavefunction $\Phi_f^{\mathbf{k}}$ is in the mirror plane, it has even-parity under reflection, therefore the resulting selection rules on the matrix element

can be written as:

$$\begin{cases} \text{if} \quad \Phi_i^{\mathbf{k}} \quad \text{even} \quad \rightarrow \quad \epsilon \cdot \mathbf{A} \text{ even} \\ \text{if} \quad \Phi_i^{\mathbf{k}} \quad \text{odd} \quad \rightarrow \quad \epsilon \cdot \mathbf{A} \text{ odd} \end{cases} \tag{3.19}$$

The relations 3.19 show that both the initial state $\Phi_f^{\mathbf{k}}$ and the interaction operator $\epsilon \cdot \mathbf{A}$ must have specific symmetries in order to exhibit a non-vanishing photoemission signal at the detector.

The matrix element is also strongly affected by the photon energy. By changing the energy of the incoming light, the kinetic energy and momentum of the photoelectrons also change, often leading to a series of minimum in the photoionization cross-section that takes the name of Cooper minima [28].

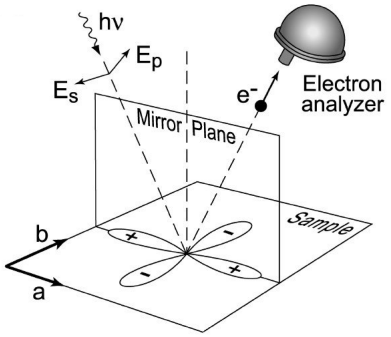


Figure 3.5: Geometrical and symmetry considerations about the photoemission process from a $d_{x^2-y^2}$ orbital [27].

At this point, it has to be stressed that both the *three-step model* and the *sudden limit* are approximations theoretically derived to facilitate the understanding of the main features of the photoemission process. Unfortunately, they are sometimes limitated and unable to provide a detailed analysis of the process. In fact, if the photoelectron has a low kinetic energy, the response of the system to the removal of the photoelectron is not negligible and the *adiabatic approximation*, in which the total final state ψ_f^N is no longer factorized into two independent terms, must be adopted. Furthermore, only the use of the *one-step model*, in which the photoemission process is described as a single event (taking into account the multiple scattering events, the matrix element effects and the surface discontinuity), allows a more specific analysis of the ARPES data. These two points become particularly critical in the context of this thesis. In fact, we exploited very low photon energy as produced by laser harmonics to perform our experiments (as described in the next sections), and the understanding of the change in the dichroic signal, discussed in Chapter 5, relies on the comprehension of final state effects.

3.4 Time-resolved ARPES

Angle Resolved Photoemission Spectroscopy represents a powerful technique for the analysis of the electronic band structure of solids. The investigation of the time-dependent electronic structure is made possible by the development of the time-resolved ARPES (tr-ARPES). The main advantage of a time-resolved approach is the ability to disentangle different processes (each of which act on a peculiar time scale) that at equilibrium coexist on the same energy scale.

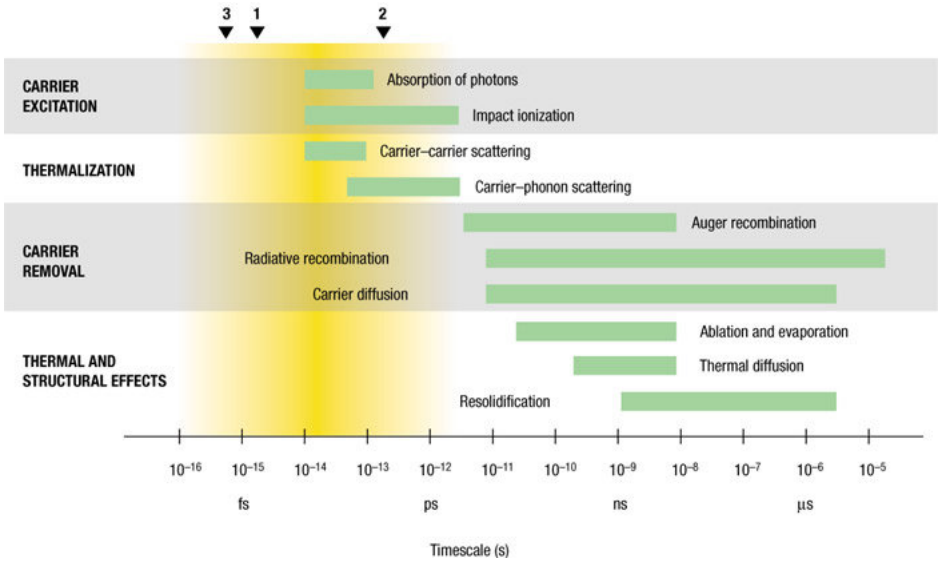


Figure 3.6: Timescales of the different carrier and lattice processes following ultrafast excitation [29].

The different steps of the relaxation undertaken by a material excited by an ultrashort laser pulse are displayed in Figure 3.6 [29]. The carrier excitation, triggered by the absorption of the photons of the ultrashort laser pulses, is the fastest process. Then, on a fs time scale the carrier-carrier scattering is responsible for redistributing the total energy of the excited system, leading to a hot thermalized carrier distribution. During the third step, the electrons lose energy to the lattice thanks to the carrier-phonon scattering. In this process the time scale can vary, according to the specific electron-phonon coupling constant, from few ps up to hundreds of ps. Once the equilibrium between the carriers and the lattice is reached, the extra energy introduced in the system by the laser pulse is removed by the process of recombination and carrier diffusion. The final step involves the relaxation due to the thermal and structural effects, that act in the solid on a longer timescale (from few ns to several μs).

Since we are particularly interested in the dynamics governed by the electron-phonon scattering, ultrashort laser pulses must be used to study the non-

equilibrium interactions. Moreover, by using pulses characterized by a photon energy in the UV region (commonly between 5.5 eV and 9 eV), it is possible to obtain high energy and angular resolutions.

3.4.1 Pump-Probe technique

The tr-ARPES technique is based on the pump-probe approach, which exploits two synchronized pulses, called *pump* and *probe* beams. The pump beam excites the sample into a non-equilibrium condition, while the probe beam is used to measure, as a function of the time delay from the pump, the effect induced by the excitation on one quantity of interest. The time delay between the two pulses is controlled by introducing a relative difference in their optical paths. This is usually obtained with a mechanical delay line set on the pump optical path: considering the speed of light, a step of 1 μm corresponds to a time delay of $\sim$6.6 fs.

The time-resolved experiments were made possible by the advent of pulsed laser sources able to produce ultrashort laser pulses ($<$ 100 fs), typically in the near-IR region. In a pump-probe experiment, the pump beam is often the fundamental of the laser source, while different probe beams can be obtain by non-linear optical processes, such as the High Harmonics Generation (HHG) and the Optical Parameter Amplification (OPA).

3.4.2 Laser system

To perform tr-ARPES experiment an ultrafast laser system producing a train of ultrashort-light pulses, with a temporal duration of $\sim$ 100 fs, is necessary. In addition to the pulse temporal duration, the other two important parameters of the laser source are the pulse photon energy (or wavelenght) and the repetition rate, measured in Hz and defined as the number of pulses per unit of time.

The laser system used in this work is sketched in Figure 3.7. A Coherent Mira oscillator, in which the active medium is a Ti:Sapphire crystal (Titanium doped Al_2O_3), is pumped by a Coherent Verdi V18 solid state laser. The pulses produced by the oscillator are amplified in a regenerative amplifier (Coherent RegA 9050) and then compressed. The repetition rate of the source is 250 kHz and the output pulses have a temporal duration of approximately 60 fs with a spectrum centered at 800 nm, corresponding to $\sim$ 1.55 eV.

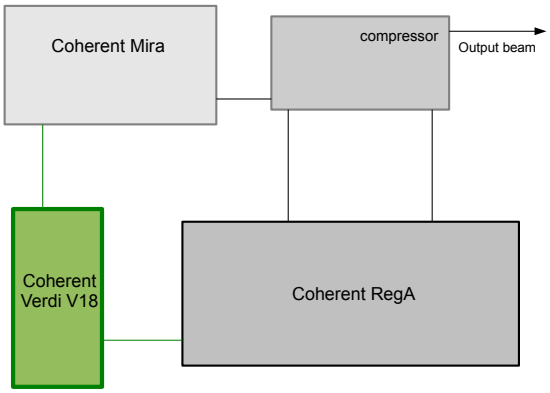


Figure 3.7: Scheme of the laser system used in the experimental setup.

3.4.3 Pump-Probe setup

In our experiments the pump beam was the fundamental of the laser source described above. For the probe beam, we used the fourth harmonics of the fundamental at 800 nm. This choice is due to the fact that we are interested in direct photoemission studies, thus the photon energy must be higher than the work function of the material, typically between $4-5$ eV. The fourth harmonics is the lowest harmonics that satisfies this requirement. To obtain ultrashort fourth harmonics pulses, we generated the fourth harmonics beam by processes of Sum Frequency Generation in phase-matched BBO crystals.

The scheme of the optical setup generating the pump and probe beams is shown in Figure 3.8. An incoming fundamental beam at 800 nm produced by the laser system is divided in two beams by the beam splitter BS1: the reflected beam represents the pump beam, while the transmitted one is used to generate the fourth harmonic beam. After the mirrors M1 and M2, the transmitted beam passes through the beam splitter BS2 and then is focalized by lens L1 on the SHG crystal (BBO crystal, type I) for second harmonic generation. The second harmonic (SH) and fundamental (F) beams are separated in two different optical paths by the separator S1, which is characterized by an high transmittance for the fundamental wavelenght and an high reflectance for the SH wavelenght. After mirror M6, the polarizer P rotates horizontal polarization of the fundamental beam to the vertical one, the same of the second harmonic beam, and then the F and SH are recombined on the separator S2. The second harmonic beam path is tuned using the M9-M10 delay line, to make the fundamental and SH beam coincident in time on the BBO crystal (type I), indicated by THG, for the sum frequency generation process. The third harmonic beam interacts in the FHG crystal (BBO, type I) with the fundamental beam coming from the M3-M4 delay line and separator S3, producing fourth harmonic. The fourth

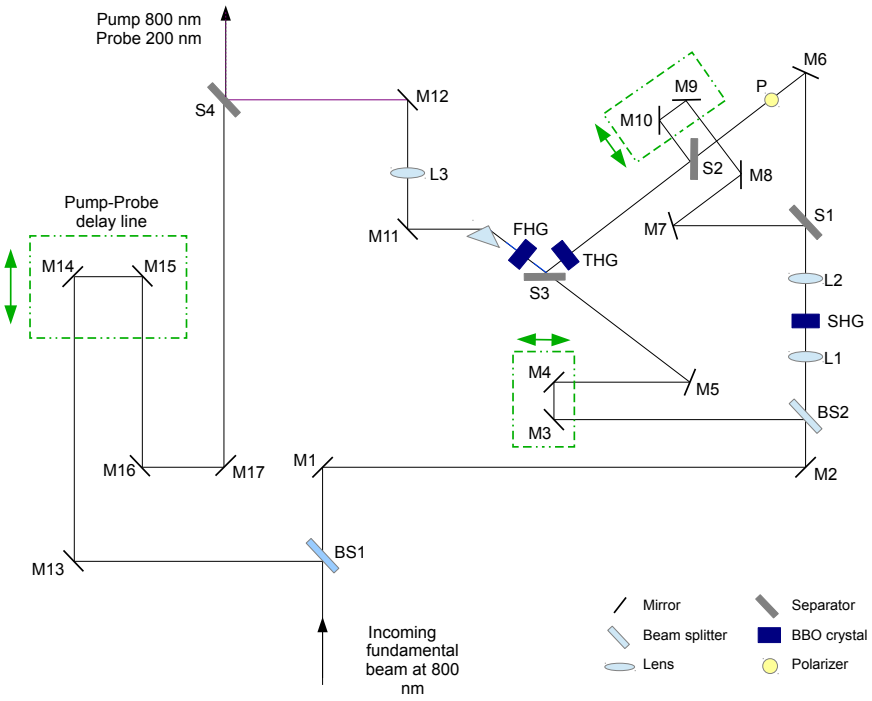


Figure 3.8: Scheme of the pump-probe optical setup.

harmonic is selected using a prism and then M11 and M12 mirrors reflect the probe beam on separator S4, where it is combined with the pump beam coming from the Pump-Probe delay line.

After separator S4, a lens focus the pump beam at 800 nm and the probe beam at 200 nm on the sample held in the UHV chamber.

3.4.4 Characterization of the probe pulse

The investigation of the electronic structure of the solid is carried out with the probe pulse. Hence, its spectral and temporal characterization is fundamental, because these quantities define respectively the energy and temporal resolution of the tr-ARPES measurements.

The spectrum of the probe pulse measured by a single-grating monochromator is reported in Figure 3.9. It is characterized by a central wavelength $\lambda = 196.80\,\text{nm}$, with $\Delta\lambda = 0.59\,\text{nm}$. This value of λ corresponds to a peak energy of $E_{IV} = 6.2\,\text{eV}$. $\Delta\lambda$ corresponds to $\Delta E_{IV} = 18\,\text{meV}$, which sets the energy resolution of the ARPES experiments.

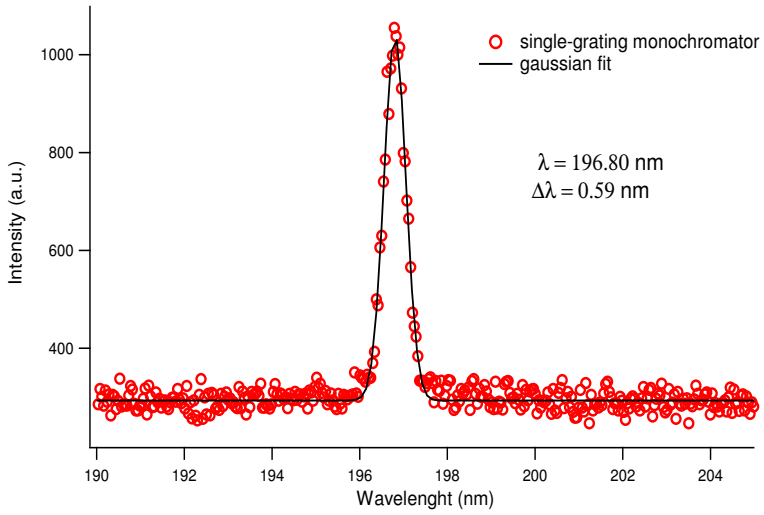


Figure 3.9: Spectrum of the fourth harmonic pulse.

In order to determine the temporal duration of the fourth harmonic pulse, a cross-correlation measurement was performed. Cross-correlation is an all-optical technique based on a non-linear second order process. In our case, a fundamental and a fourth harmonic pulse, delayed each other by Δt by introducing a difference in their optical paths, interact on a BBO non-linear crystal for generating a third harmonic pulse through the difference frequency generation process. The intensity of the resulting third harmonic pulse is given by the cross-correlation of the intensity of the two initial pulses:

$$I_{III}(t) = \int_{-\infty}^{+\infty} I_{IV}(t) I_I(t + \Delta t) dt \tag{3.20}$$

On the detector the intensity of third harmonic pulse is collected as a function of the delay between the fundamental and fourth harmonic pulses. Figure 3.10 shows the third harmonic intensity profile obtained by the cross-correlation measurement. The temporal duration of the fourth harmonic pulse is calculated by deconvolving the pump FWHM from the cross-correlation FWHM, and results equal to 330 fs. This value determines the temporal resolution of tr-ARPES experiments, i.e. the fastest dynamics that can be resolved by our measurements.

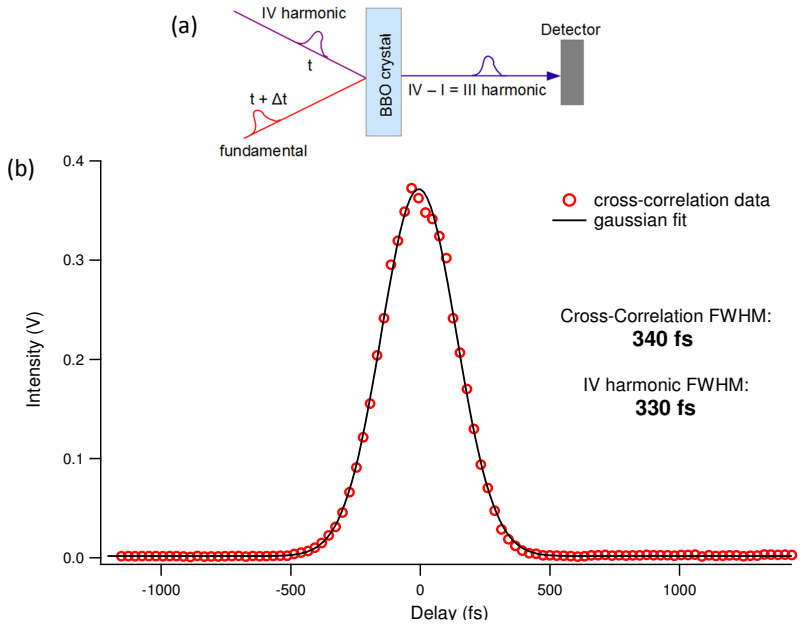


Figure 3.10: (a) scheme of the cross-correlation measurement; (b) the intensity profile of the third harmonic pulse obtained by difference frequency generation, as a function of the delay Δt between the fourth harmonic and fundamental pulses.

Chapter 4

Time-resolved ARPES measurements on BiTeI

The layered semiconductors BiTeX (with X = I, Cl, Br) exhibit a large Rashba-type spin splitting (as discussed in Chapter 2), therefore they are of particular interest for the development of spintronic devises. In this frame, the electron-phonon coupling constant, λ, is a fundamental quantity to be investigated, because electron-phonon coupling in a strongly spin-orbit coupled material dictates the transport properties. In fact, owing to the breaking of the spin degeneracy the elastic backscattering on a non magnetic impurity is forbidden, and any scattering event has to rely on the exchange of a non-zero momentum, as provided by the interaction with phonons. For these reasons, we have investigated the strength of electron-phonon interactions in BiTeI in the time domain by time-resolved ARPES.

The first part of this chapter reports the description of the experimental setup and the data collection. The second part of the chapter illustrates the analysis of the Energy Distribution Curves (EDCs) of the density of states, focusing on the temporal evolutions of the effective electronic temperature T^*_{el} and the effective chemical potential μ^* that characterize the *hot* electronic gas. The third part of the chapter presents the analysis of the Momentum Distribution Curves (MDCs). Finally, we report the measure of λ for BiTeI as resulting from the Two Temperatures Model (2TM).

4.1 Measurement conditions

High quality single crystals of BiTeI were grown by chemical vapor transport and by the Bridgman technique, and characterized by x-ray diffraction and transport by Dott. H. Berger, Dott. Ph. Bugnon and Dott. A. Magrez (at EPFL in Lausanne). The tr-ARPES experiments were performed at the T-ReX

laboratory at Elettra synchrotron in Trieste. The BiTeI samples were mounted on a six-degrees of freedom manipulator and cleaved *in situ* in ultrahigh vacuum ($p \sim 2{\cdot}10^{-10}$ mbar) at room temperature. During the measurements the samples were kept at low temperature (between 100 K and 120 K) using a LN_2 cryostat. The pump laser beam was p-polarized and it was set at 800 nm ($\sim$ 1.55 eV) with a repetition rate of 250 kHz. The adsorbed pump fluence (defined as the power of the laser pulse per unit of area adsorbed by the sample) was varied within the range between 18 μJ/cm^2 and 109 μJ/cm^2 in order to study the modification of the electronic band structure as a function of the pump fluence. Electrons were photoemitted by the s-polarized fourth harmonic at 200 nm ($\sim$ 6.2 eV), which was obtained by double harmonics generation in BBO ($\beta-$borato di bario) crystals. The photoelectrons were collected and analysed by a SPECS Phoibos 225 hemispherical spectrometer, with energy and angular resolutions respectively of 10 meV and 0.3° (corresponding to 0.0005 Å^{-1} in wave vector). The time resolution of all the experiments was set by the temporal duration of the probe pulses at $\sim$ 330 fs.

4.2 Equilibrium and non-equilibrium electronic properties of spin-split states of BiTeI

We chose to performed time-resolved experiments on BiTeI, because this system is characterized by a relatively simple band structure and it exhibits only two pairs of spin-split states near the Fermi level, having larger Rashba energy, E_R, and momentum offset k_0.

Seven data sets were collected by varying the pump fluence. This corresponds to a variation in the energy transferred by the pump in the electronic bath. A precise estimation of the parameters necessary to convert the pump fluence in energy adsorbed by the sample is given at the end of the chapter, when dealing with the Two Temperature Model. The sample base temperature and the adsorbed pump fluence for each data set are summarized in the table below.

Table 4.1: Values of temperature and fluence of the pump beam adsorbed by the sample that characterized the time resolved ARPES experiments performed on BiTeI

	Experiment						
	A	B	C	D	E	F	G
T (K)	100	100	100	120	120	120	120
Absorbed pump fluence (μJ/cm^2)	18	25	36	47	47	47	109

In each tr-ARPES experiment we investigated the electronic properties at the Fermi level along the $\overline{\Gamma K}$ high symmetry direction. Each step of the mechanical delay line, which introduces a relative difference in the optical paths between the pump and probe pulses, was of $\sim$ 15 μm corresponding to $\sim$ 100 fs.

The acquired images are organized to build a *cube*, in which the delay time is associated to the third axis, in addition to the energy and momentum axis of conventional ARPES at equilibrium.

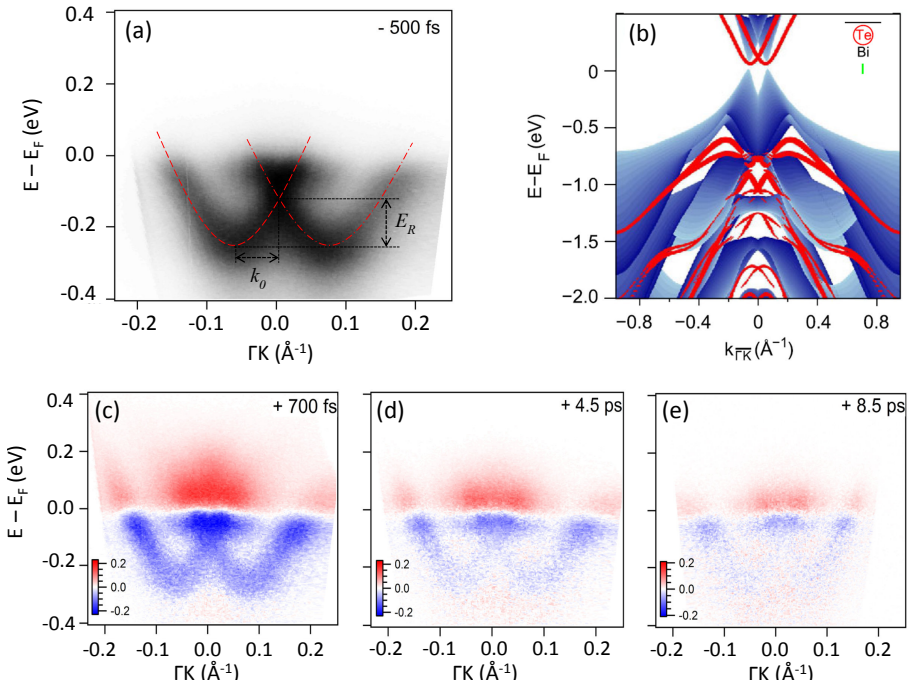


Figure 4.1: BiTeI ARPES images along the $\overline{\Gamma K}$ high symmetry direction : (a) ARPES band dispersion at negative delay time. The red curves, obtained from parabolic fit to the data, are a guides for the eyes to trace the dispersion of the surface states. These fits provide us with values of the Rashba energy and the momentum offset, equal respectively to $\sim$ 0.11 eV and $\sim$ 0.057 Å^{-1}. (b) BiTeI band dispersion calculation, where the blue continuum accounts for the projected bulk band structure, while red contours line the dispersion of the surface-derived states [25]. (c)-(e) tr-ARPES images obtained as the difference between the images at positive delay times (700 fs, 4.5 ps, 8.5 ps) and image at negative delay time (−500 fs). Blue (red) region indicates a decrease (increase) of the spectral weight.

ARPES images were collected for negative delay times (before the arrival of the pump pulse) in order to provide a reference for the electronic band structure before optical perturbation. Figure 4.1 (a) shows the band dispersion of BiTeI at

negative delay time $-500\,\text{fs}$. A pair of spin-split states is clearly resolved and the parabolic provides a Rashba energy and a momentum offset equal to $\sim 0.11\,\text{eV}$ and $\sim 0.057\,\text{Å}^{-1}$ respectively. These values suggest that the observed states can be attributed to the spin-split surface states as identified and discussed thoroughly in the work of Crepaldi *et al.* [25]. In particular, Figure 4.1(b) shows the calculated electronic properties of BiTeI, where the blue continuum accounts for the projected bulk band structure, while red contours line the dispersion of the surface-derived states.

Figures 4.1 (c)-(e) present the tr-ARPES images obtained by subtracting the photoemission intensity at negative delay time ($-500\,\text{fs}$) from the one at positive delay times ($700\,\text{fs}$, $4.5\,\text{ps}$, $8.5\,\text{ps}$ respectively). In such a way the data highlights the effects of the pump excitation on the electronic structure of BiTeI near the Fermi level are well highlighted. It is evident that due to the pump excitation a decrease of the spectral weight in the states just below E_F (the blue signal) and an increase in the states just above E_F (the red signal) occur. We interpreted this behaviour as a thermal perturbation of Fermi-Dirac distribution associated to an increase in the electron gas kinetic energy induced by the absorption of the optical pulse.

A most quantitative investigation of the dynamics of the electronic band dispersion can be performed by analysing the spectral lineshape of the spin-split surface states. In order to accomplish such analysis, two different approaches are commonly used. The first consists in analysing the *Energy Distribution Curve* (EDC), so the photoemission signal as a function of the photoelectron kinetic energy. The second consists in fixing the binding energy and analysing the behaviour of the photoemission intensity as a function of the momentum, the so-called *Momentum Distribution Curve* (MDC).

4.3 EDCs analysis of the density of states

The photoemission intensity is proportional to the $A(\mathbf{k}, h\omega, t) \cdot f(h\omega, t)$, where the former represents the one-particle spectral function and the latter the Fermi-Dirac distribution. Contrary to the ARPES experiment at equilibrium, when dealing with tr-ARPES measurements the time dependency has to be taken into account. We notice that the time-dependent Fermi-Dirac distribution is independent from the wave vector $\mathbf{k}$, so its analysis is easily accessible in the energy domain. Hence, in this section we focus on the EDCs analysis of the density of states in order to investigate the perturbation of the Fermi-Dirac distribution due to the optical excitation. This analysis provides information on the relaxation of the energy transferred from the carriers to the lattice. In particular, it provides a measure of the electron-phonon coupling strength of the material. In the next section we face the intriguing problem of extracting information about the microscopic scattering mechanism, such as the quasiparticles lifetime, by studying the dynamics of the $\mathbf{k}$-dependent $A(\mathbf{k}, h\omega, t)$ through the MDCs analysis.

In our study we adopted a method for the time dependent EDCs analyis slightly different with respect to the one conventionally performed in ARPES experiment at equilibrium. In fact, the standard EDCs analysis at specific fixed momentum only considers a limited region of the band dispersion (in our case, for example, in the vicinity of E_F, k_F). Therefore, this approach does not consider the transfer of the spectral weight occurring along the whole parabolic dispersion during the pump excitation and the subsequent relaxation. A strategy to overcome this shortcoming is to integrate the ARPES signal in momentum along the band dispersion, thus extracting the density of states relative to the specific states as a function of its biding energy as proposed by Wang *et al.* [30] for studying the out-of-equilibrium electronic properties of topological insulators.

Our analysis is focused on the outer branch of the left parabola by integrating the photoemission intensity $I(E, \mathbf{k}, t)$ in a small interval along the parabolic dispersion (red lines in Figures 4.2 (a)), in order to obtain the density of states as a function of the delay time (Figures 4.2 (b)). Figures 4.2 (c)-(f) display the EDCs corresponding to four selected delay times $-500\,\mathrm{fs}$, $700\,\mathrm{fs}$, $4.5\,\mathrm{ps}$, $8.5\,\mathrm{ps}$ respectively. It is clear that the pump excitation causes a sudden modification of the *slope* of the Fermi-Dirac distribution, which is interpreted as an increase of the electronic temperature. This effect is highlighted in Figure 4.2 (h), where the EDCs fitting curves at positive delay time ($-500\,\mathrm{fs}$) are compared to the one at negative delay time, and the shadow areas indicate the transfer of spectral weight occurring near the Fermi level.

For each time delay, the EDC was fitted with the following model function:

$$\Upsilon(E,t) = \frac{A(t)}{1+\exp[(E-\mu^*(t))/(k_B T^*_{el}(t))]} \cdot \xi(E) + \Phi \tag{4.1}$$

The EDCs curves are approximated by the product between the Fermi-Dirac distribution, characterized by the effective temperature T^*_{el} and the effective chemical potential μ^*, and a second order polynomial $\xi(E)$ describing the density of states relative to the state. Moreover, in Equation 4.1, k_B is the Boltzamann costant, A is a time-dependent normalization factor of the photoemission intensity, as it is explained more in detail in the following, and Φ is the background for energies above E_F.

Φ and $\xi(E)$ were determined by fitting the first EDC of the serie (at negative delay time) and they were hold them fixed for all the time delays.

We determined the normalization factor by integrating the area below the EDCs in an interval of $200\,\mathrm{meV}$ centered around the Fermi level. In fact, in first approximation, neglecting the shift of the chemical potential, the thermal modification of the Fermi-Dirac distribution is *symmetric* around E_F (the spectral weight lost below E_F is gained above E_F), so the integrated area is conserved. At a second level of approximation, we have taken into account that the value of the effective chemical potential can slightly change during both the excitation and the relaxation. Therefore, we developed an iterative procedure to calculate $A(t)$. In the first iteration cycle, we centered the integration interval around the

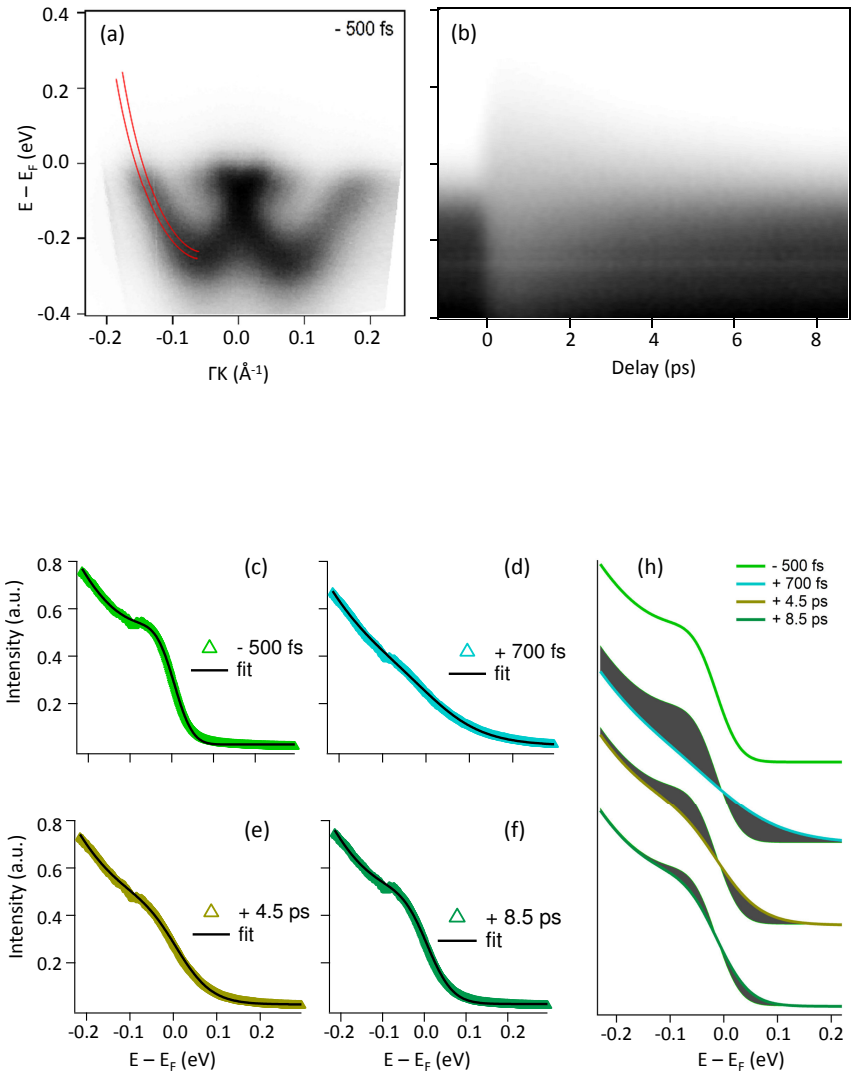


Figure 4.2: (a) tr-ARPES images along $\overline{\Gamma K}$ at negative delay time (−500 fs). The red lines show the momentum range where the photoemission intensity was integrated to obtain the partial density of states as a function of delay time (b); (c)-(f) EDCs at four selected delay times: −500 fs, 700 fs, 4.5 ps, 8.5 ps respectively. The fitting curves, black lines, are the result of the product between the Fermi-Dirac distribution and a second order polynomial, convoluted with a gaussian to account for the experimental resolution; (g) comparison between the density at negative delay time (−500 fs) and positive delay times. It is evident the transfer of spectral weight from below to above E_F.

value of the chemical potential. The same integration interval was used to calculate the normalization factor for all the EDCs of the same experiment. Once extracted these $A(t)$ values, we fitted the EDCs using the model function $\Upsilon(E,t)$ of equation 4.1, obtaining the time dependent effective chemical potential for each delay time. As so, a new calculation of $A(t)$ was carried out by integrating each EDC around its time dependent chemical potential, extracted from the previous iteration cycle. We repeated the above procedure several times until the difference in the $A(t)$ values extracted from two consecutive iterative cycles was smaller than 0.5%. Figure 4.3 (a) shows an example of $A(t)$ as obtained with this iterative procedure. The three A-curves represent the different iterative cycles, while Figure 4.3 (b) presents the estimated modification of $A(t)$ between two immediately subsequent iterative cycles.

We extracted the temporal evolution of T^*_{el} and μ^* from the fit of the EDCs using the model function $\Upsilon(E,t)$ and the analysis of their temporal evolution is the subject of the next paragraphs.

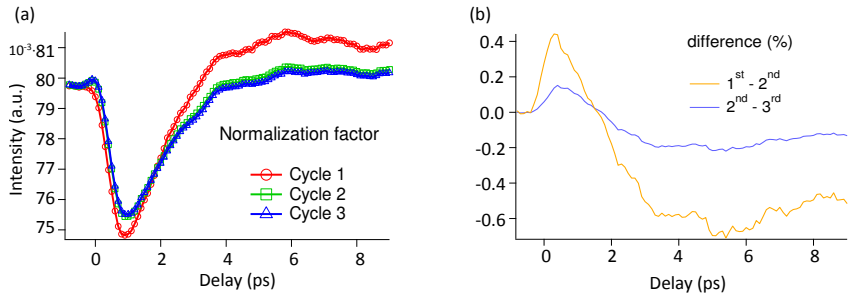


Figure 4.3: (a) Values of the normalization factor $A(t)$ of the photoemission intensity obtained in three different cycles of the iterative procedure; (b) estimated modification of $A(t)$ values between two consecutive iterative cycles.

4.3.1 Evolution of the effective electronic temperature T^*_{el}

Figure 4.4 shows the values of the effective electronic temperature obtained in the case for an absorbed pump of $\sim 47\,(\mu\mathrm{J/cm^2})$. The black and the green lines refer to the outer and inner branches of the surface states, respectively. The analytical form the polynomial $\xi(E)$ is different for the two branches, owing to matrix element effect and also reflecting the different behaviour of the associated density of states, but it is important to notice that the resulting T^*_{el} evolution is the same.

The same analysis was performed for the various pump fluences. Figure 4.5 illustrates the dynamics of T^*_{el} for the seven experiments reported our study, while the inset shows the maximum values of T^*_{el}. The increase of the maximum

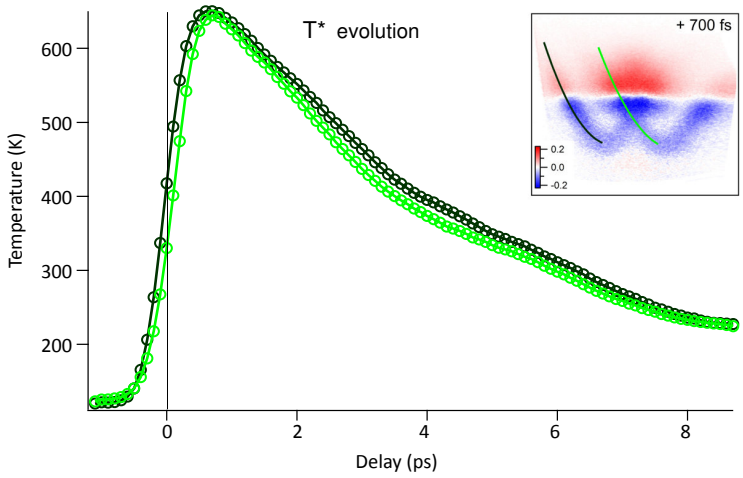


Figure 4.4: Temporal evolution of the effective electronic temperature T_{el}^{*} resulting from the fit of the EDCs using the function $\Upsilon(E)$. The two curves refer to the outer and inner branches of the surface states shown in the inset by black and green lines. The maximum value of T_{el}^{*} and the temporal evolution are approximately the same for the two curves.

T_{el}^{*} reflects the increase of the energy transferred to the sample by the pump pulse. An increase of six times in the absorbed pump fluence (from $\sim 20\,\mu\mathrm{J/cm^2}$ to $\sim 110\,\mu\mathrm{J/cm^2}$ for experiment A and G respectively) results in the doubling of T_{el}^{*} maximum (from $\sim 430\,\mathrm{K}$ to $\sim 830\,\mathrm{K}$).

A more detailed insight into the dynamics of the relaxation process, occurring after the pump excitation, is obtained from a quantitative analysis of the temporal evolutions of T_{el}^{*} as shown in Figure 4.5.

The dynamics of T_{el}^{*} was fitted with the function $\Lambda(t)$ expressed as,

$$\Lambda(t) = \int_{-\infty}^{+\infty} \Theta(t^{'}) \cdot G(t^{'} - t) \cdot C \, \exp\left(-\frac{t^{'}}{\tau_T}\right) \, dt^{'} + \Xi \tag{4.2}$$

The function $\Lambda(t)$ is the convolution between a single decay exponential and a gaussian G accounting for the temporal resolution of our measurements. Θ represents the proper rise-time, modelled through a step-function, of the single decay exponential describing the relaxation of the *hot* carriers. Finally, the intensity normalization C identifies the maximum value of T_{el}^{*} and Ξ is a background that takes into account the sample base temperature before the arriving of the pump pulse. In this approximation, the temporal evolution of T_{el}^{*} is uniquely determined by the relaxation time τ_T that provides the time scale of the relaxation mechanism.

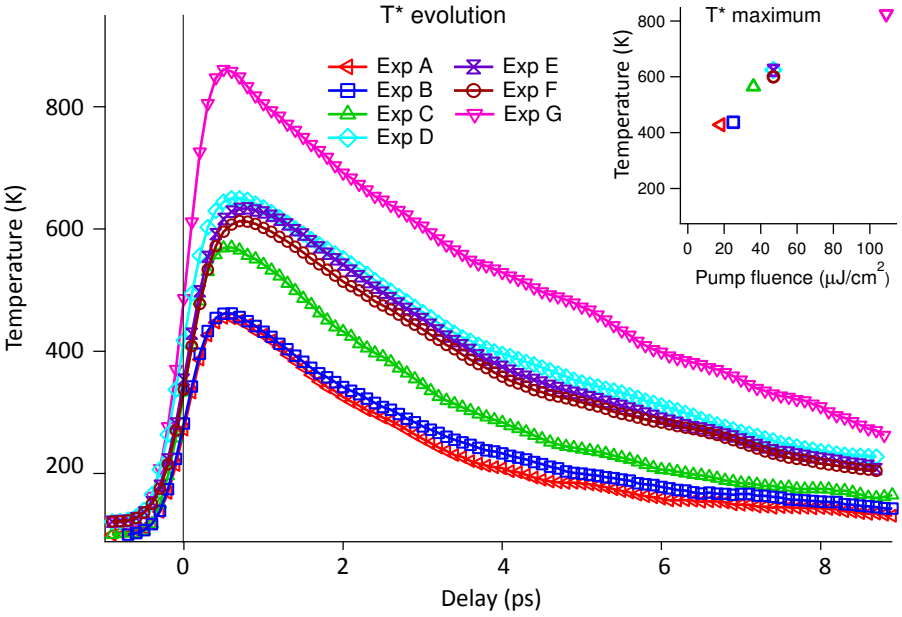


Figure 4.5: Temporal evolution of the effective electronic temperature T_{el}^{*} for all tr-ARPES experiments performed. The difference in the absorbed pump fluence is reflected in the increase of the maximum value of T_{el}^{*} (inset).

We used the $\Lambda(t)$ function to fit all the T_{el}^{*} curves displayed in Figure 4.5. The resulting fits are presented as black lines in Figure 4.6, and they well approximate the experimental data. The values of the relaxation times extracted from these fits for the different pump fluences are reported in Table 4.2.

Table 4.2: Values of the relaxation time τ_T for the different pump fluences, as obtained from the fit of the T_{el}^{*} temporal evolution curves using the $\Lambda(t)$ function.

	Experiment						
	A	B	C	D	E	F	G
Adsorbed pump fluence (μJ/cm^2)	18	25	36	47	47	47	109
τ_T (ps)	2.9	3.4	3.6	4.9	4.5	4.5	5.5

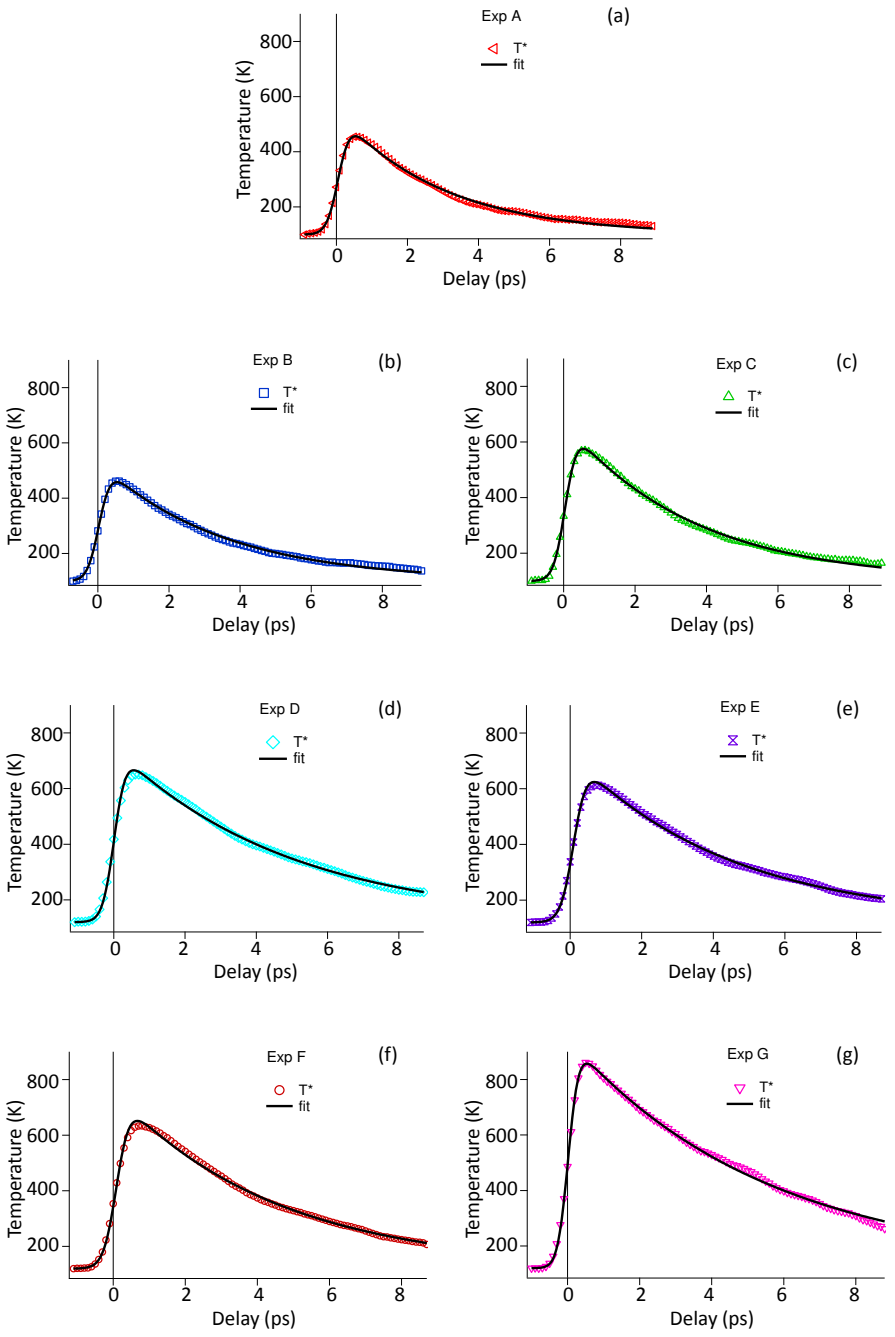


Figure 4.6: Temporal evolution of the effective temperature T_{el}^{*} fitted with a single exponential decay convoluted with a gaussian.

It is interesting to notice that τ_T is not the same for all the experiments. The different values of τ_T, summarized in Figure 4.7, indicate that the relaxation time increases along with the increase of the pump fluence. In particular, an increase of six times of the pump fluence results in an almost doubling increase of τ_T (from 2.9 ps to 5.5 ps).

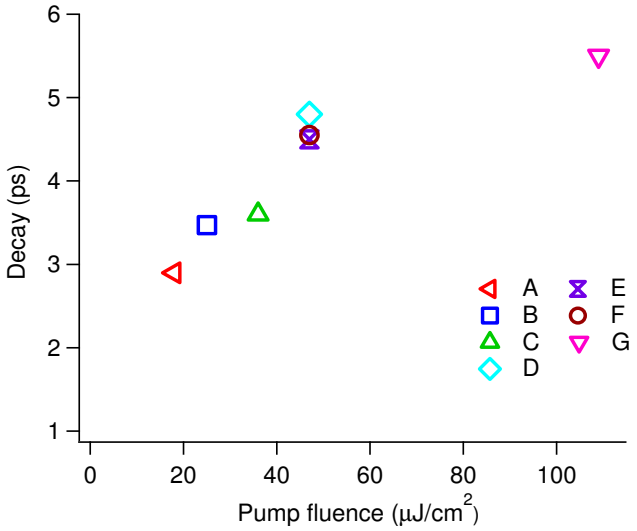


Figure 4.7: Values of the relaxation time characterizing the temporal evolutions of T^*_{el} for the different adsorbed pump fluence. The characteristic relaxation time increases as a function of the pump fluence.

If the relaxation of T^*_{el} was only due to the electron-phonon scattering processes, the value of the characteristic relaxation time would have been the same when varying the adsorbed pump fluence. The fluence-dependence of τ_T suggests that other contributions to the relaxation of T^*_{el} must be included in the model. The slowdown of the T^*_{el} relaxation may arise from effects of carriers diffusion or from the formation of electron-hole pairs, that is an important effect to be considered for the physics of semiconductors. This mechanisms can be reflected in a bottleneck in the relaxation channels for the carriers optically excited by the pump pulse from the valence band into the conduction band. Similar tr-ARPES studies of the surface state of topological insulators Bi_2Se_3 [31] and Bi_2Te_3 [32] resolved a long-lasting signal above the Fermi level. The authors proposed the idea that the conduction band acts as a charge reservoir for the topological surface state at lower binding energies, resulting in a persistent non-equilibrium population. In fact, the presence of a band gap of the order of hundred meV makes the electron-phonon scattering unavailable for the recombination of the excited electrons with the valence band holes. For this reason, the authors proposed that the surface states act as intermediate states in the en-

ergy relaxation between the conduction and valence bands, therefore the surface states are subjected to a continuous charges filling from the conduction band at larger binding energy. This argument, can be generalized to other small gap semiconductors, and it constitutes our first step towards a better understanding of the slowdown of the relaxation of T_{el}^{*} observed in BiTeI when increasing the pump fluence.

4.3.2 Evolution of the effective chemical potential μ^*

The dynamics of μ^*, as extracted from the EDCs analysis, are shown in Figure 4.8 with the corresponding fits (black lines). Similarly to T_{el}^{*}, the temporal evolution of μ^* was fitted with a single decay exponential convoluted with a gaussian to account for the temporal resolution. Figure 4.8 shows that after the pump excitation, the value of the effective chemical potential slightly decreases, with the exception of the experiment A. In this case μ^* exhibits a positive shift, which is smaller in absolute value than in the others experiments, furthermore this shift is smaller or comparable with the experimental energy resolution. The absolute value of the maximum variation of μ^*, $\Delta\mu^*$, occurring in each experiment are presented in Table 4.3. With the exception of the experiment A, the values of $\Delta\mu^*$, as obtained from different experiment, are comparable, suggesting that $\Delta\mu^*$ is independent on the pump fluence. Table 4.3 also reported the characteristic relaxation time τ_μ, and, likewise T_{el}^{*}, the value is not the same in all the experiments. However, even if the minimum and maximum values of τ_μ are associated respectively to the minimum ad maximum pump fluences, the behaviour of τ_μ does not present a clear trend when increasing the pump fluence, in contrast to what previously discussed for T_{el}^{*}.

Table 4.3: Absolute values of the maximum variation of μ^*, $\Delta\mu^*$, and the characteristic relaxation time τ_μ for different adsorbed pump fluences.

	Experiment						
	A	B	C	D	E	F	G
Adsorbed pump fluence (μJ/cm^2)	18	25	36	47	47	47	109
$\Delta\mu^*$ (meV)	5	16	16	17	18	14	14
τ_μ (ps)	1.4	2.3	3.1	3.0	2.7	2.0	4.8

The negative shift we observed is small (< 20 meV) but not negligible. An ultrafast shift of the effective chemical potential has been recently revealed in the topological insulator Bi_2Se_3 by several groups [33, 30]. They observed a positive shift that was interpreted as a consequence of the ultrafast photodoping of the conduction band. Conversely, we observed a negative shift of μ^*, which cannot be attributed neither to a photodoping effect, nor to a thermal effect,

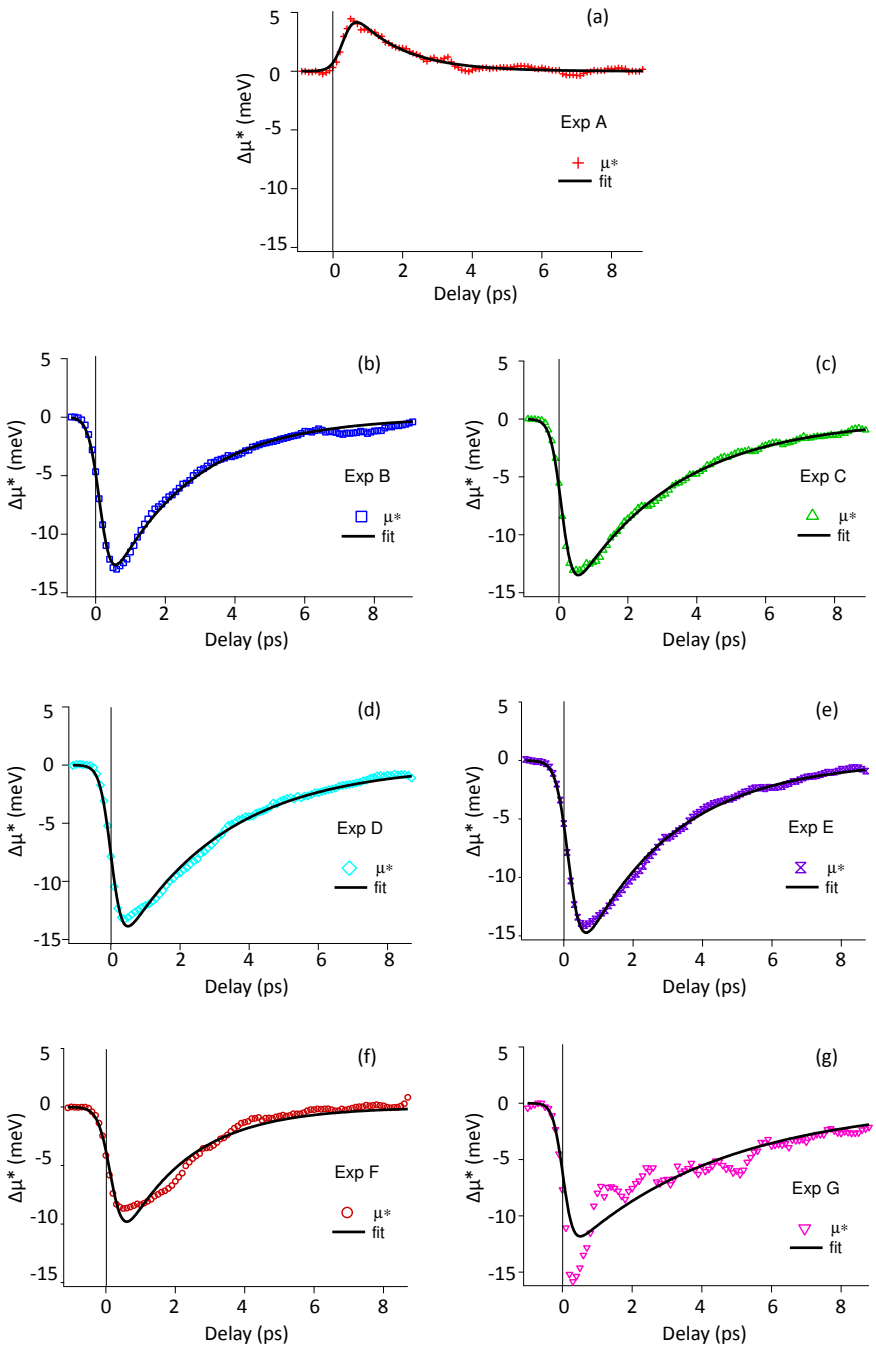


Figure 4.8: Temporal evolution of the effective chemical potential μ^* fitted with a single exponential decay convoluted with a gaussian.

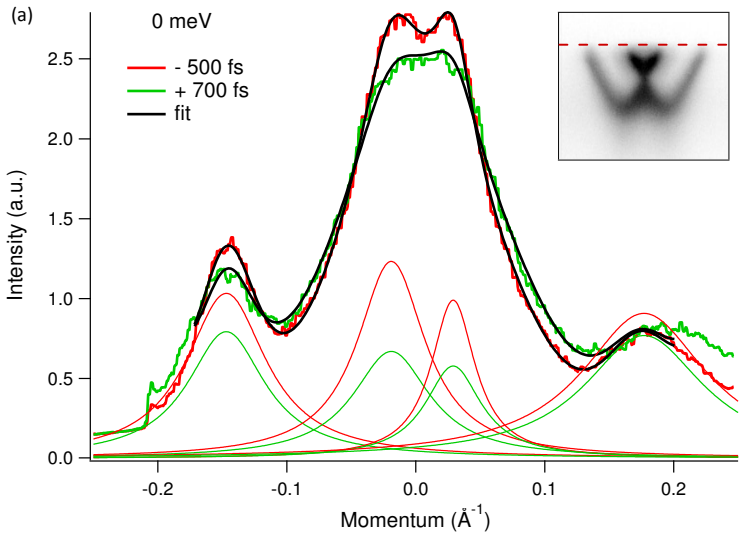
because in latter case μ^* would be characterized by a positive shift, according to the analytic form of the density of states in the spin-split states (proportional to $\sim E^{-\frac{1}{2}}$).

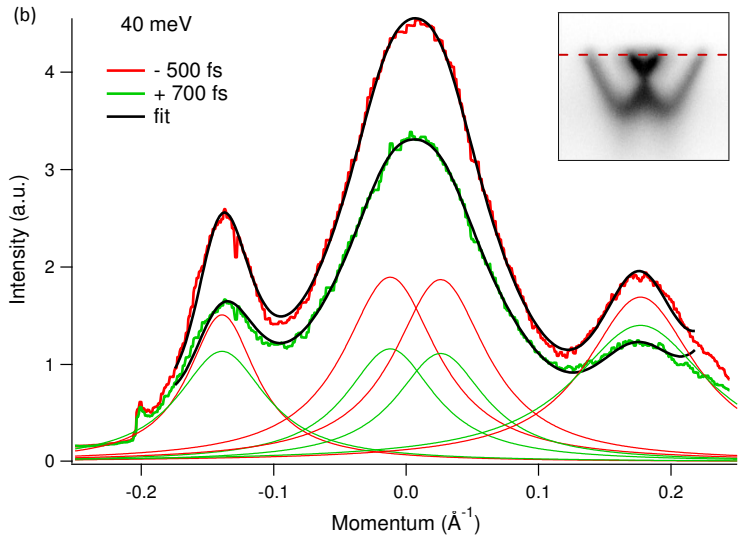
The negative shift of μ^* can be interpreted as an effect of the diffusion of the carriers out of the probed volume or it can be considered a consequence of the fact that the electrons excited in the conduction band with high energy have higher mobility. As a result, they can delocalize in different region of the surface and locally be trapped by the positive charges of the bilayer $(BiTe)^+$.

4.4 MDCs analysis

In the previous section we focussed on the analysis of the Fermi-Dirac distribution term appearing in the expression of the photoemission intensity. Instead, this section is dedicated to the analysis of the dynamics of the one-particle spectral function $A(\mathbf{k}, h\omega, t)$ through the MDCs, in order to obtain information on the microscopic scattering mechanisms by using the theoretical models briefly introduced in Chapter 3. In particular, the MDCs analysis provides information on the quasiparticle lifetime. This kind of analysis has been applied to tr-ARPES data for the first time by Johannsen *et al.* in the case of quasifree standing graphene and it enable them to disentangle the role of various one-particle scattering mechanisms [34].

Here we analysed the MDCs by integrating, for each time delay, the photomission intensity in a small energy interval (10 meV) centred at four selected binding energies, 0 meV, 40 meV, 80 meV, 140 meV. Figure 4.9 shows the MDCs obtained at two different delay times. The red curve corresponds to a negative delay time (−500 fs), while the green curve corresponds to a positive delay time (+700 fs). To quantitatively evaluate the modification of the MDCs, the integrated photoemission intensity was fitted with a parabolic background and four lorentzians describing the quasiparticle peaks in the inner and outer branches of the two parabolas. The four lorentzian contributions are shown in the graphs. Here we focus our discussion on the outer branch of the left parabola. By extracting the full width at half maximum (FWHM) of the lorentzian peak at each delay time, information on the dynamics of the quasiparticle lifetime is obtained of the FWHM, as briefly discussed in Chapter 3. The temporal evolutions of the FWHM corresponding to the different binding energies are shown in Figure 4.10. It is evident that at E_F the value of the FWHM is roughly constant, while at different binding energies it shows a temporal evolution. We fitted the relaxation below E_F with a single decay exponential, convolved with a gaussian, and we extracted the characteristic decay time, τ_l. Table 4.4 reports the values of τ_l corresponding to the selected binding energies for different absorbed pump fluences.


(a)
0 meV
- 500 fs
+ 700 fs
fit
Intensity (a.u.)
Momentum (Å^{-1})


(b)
40 meV
- 500 fs
+ 700 fs
fit
Intensity (a.u.)
Momentum (Å^{-1})

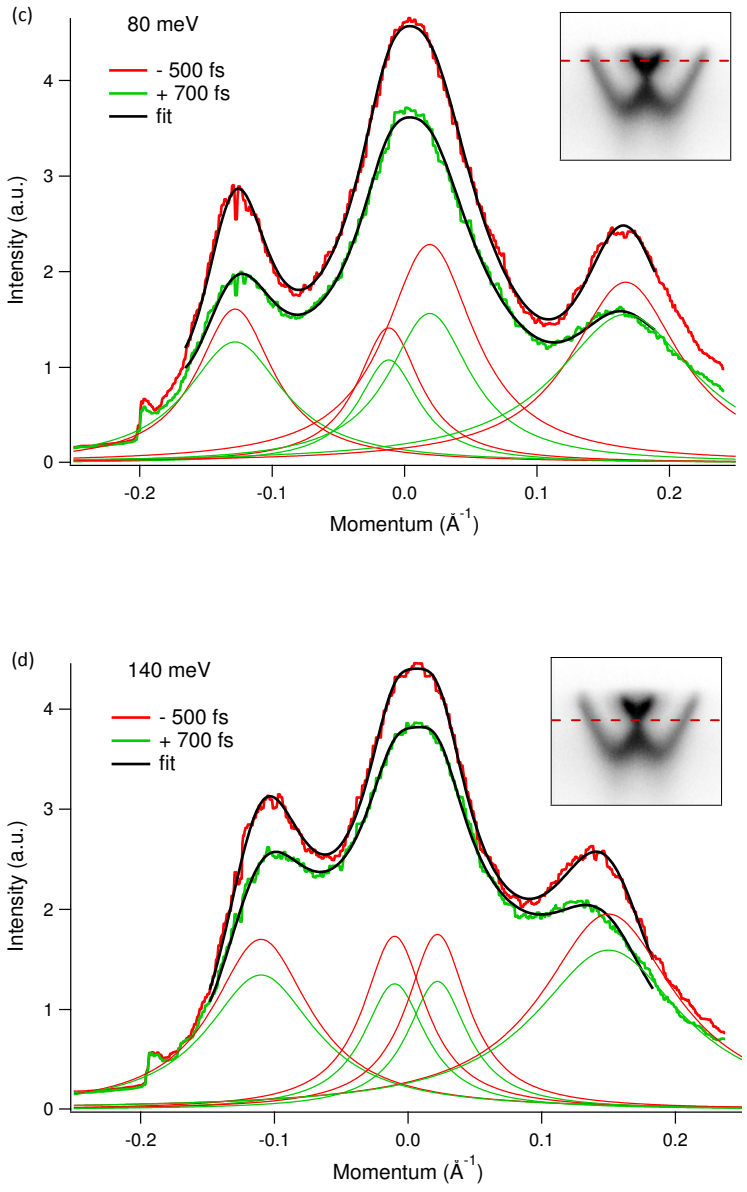


Figure 4.9: Momentum Distribution Curves extracted at four different binding energies (0 meV, 40 meV, 80 meV, 140 meV respectively). The red curve corresponds to a negative delay time (−500 fs), while the green curve corresponds to a positive delay time (+700 fs). The fit (black line) is the result of the convolution of four lorentzians (the deconvolved lorentzian are shown in the graphs without the background).

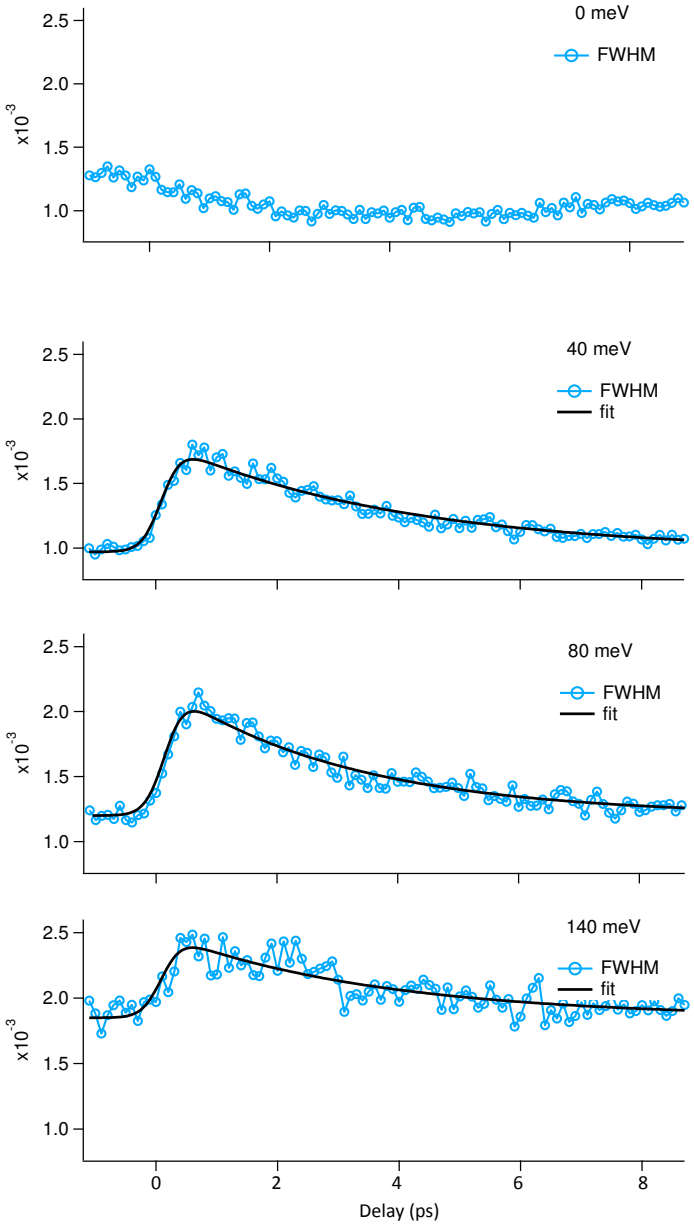


Figure 4.10: Temporal evolution of the FWHM of the left lorentzian peak extracted from the four selected binding energies (0 meV, 40 meV, 80 meV, 140 meV respectively). The black lines are the results of the fit obtained with a single exponential decay convoluted with a gaussian.

Table 4.4: Values of the characteristic relaxation time τ_l for different adsorbed pump fluences.

		Adsorbed pump fluence (μJ/cm^2)			
Binding energy (meV)		36	47	47	109
40		3.5	3.8	4.4	3.1
80	τ_l (ps)	2.2	3.1	3.4	4.3
140		2.5	3.5	4.2	3.2

Interestingly, the values of τ_l do not exhibit a clear trend when increasing the adsorbed pump fluence and the binding energies. In particular, it is clear from Table 4.4 that the dynamics of the FWHM obtained by the MDCs analysis results different from the one characterizing the T_{el}^* (extracted through the EDCs analysis).

Further investigations are necessary to understand in details the cause of the modifications of τ_l, thing that is currently beyond the scope of this thesis. Here, we want to highlight that this powerful analysis, complementary to the EDCs, can be performed on these Rashba-type materials, as already done for the graphene [34], and that it may provide novel information on the microscopic scattering mechanisms.

4.5 Electron-Phonon coupling in the spin-split states of BiTeI

After the electrons are optically excited in a strongly out-of-equilibrium state by ultrashort light pulses, they recover a thermalized electronic distribution through electron-electron anharmonic scattering processes and transfer their excess energy to the rest of the system mainly through electron-phonon scattering processes. The time scale of electron-electron scattering processes is of the order of few fs, beyond the temporal resolution of conventional time-resolved experiments. On the contrary, the electron-phonon scattering occurs on the time scale of few ps, therefore it can be resolved. The characteristic relaxation time required to restore an equilibrium condition between the electrons and the lattice depends on the strength of the electron-phonon interaction.

By using the information on the temporal evolution of the effective electronic temperature presented in Section 4.3.1, it is possible to derive the electron-phonon coupling constant in BiTeI. Such result is achieved by adopting the 2TM, widely used to extract the electron-phonon coupling strength from measurements in the time-domain.

4.5.1 The Two Temperatures Model

The 2TM was developed by Anisimov [35] and Allen [36] and it describes the transfer of the energy between the electrons and the lattice. The 2TM neglects any other collision processes except for the electron-phonon process, it neglects spatial diffusion and assumes an homogeneous laser excitation.

When the sample is excited by a pump pulse, a non-equilibrium state between electrons and the lattice is created. In fact, the electrons absorb all the energy deposited into the sample by the laser pulse, leaving the lattice at essentially the same temperature it had before the excitation. As a result, the electrons are instantaneously excited above the Fermi level, and their energy is redistributed among them through electron-electron scattering on a fs time scale ($\sim$ 10 fs [37]). This process creates a thermalized electron distribution, characterized by a temperature $T_{el} > T_L$ where T_{el} and T_L represents the temperature of the electronic distribution and the lattice respectively. The name Two Temperatures Model recalls that for each of the two interacting subsytems (electrons and phonons), a temperature has been defined. With the fundamental assumption that the electron-electron and the phonon-phonon (anharmonic) processes are much faster than the electron-phonon processes, the electronic and phononic distributions can be considered equal to their local equilibrium distribution (Fermi-Dirac and Bose-Einstein respectively) described by the following expressions [38]:

$$\begin{aligned} &\text{for electrons:} \quad N_k = \frac{1}{\exp[\beta_{el}(\epsilon - \epsilon_0)] + 1} \qquad \text{with } \beta_{el} = \frac{1}{k_B T_{el}} \\ &\text{for phonons:} \quad N_f = \frac{1}{\exp[\beta \hbar \omega_f] - 1} \qquad \text{with } \beta = \frac{1}{k_B T_L} \end{aligned} \tag{4.3}$$

On a time scale of few ps the electrons cool down by transferring the extra energy to the lattice, via electron-phonon interactions, till they reach the equilibrium.

When the decay process is governed solely by the electron-phonon scattering, the 2TM can be used to extract λ by analyzing the relaxation of the electronic temperature in the time domain.

In 1974 Anisimov proposed a system of coupled differential equations describing the evolution of the electronic and the lattice temperatures after a laser pulse excitation. The equation expressing the rate of energy loss from the electrons to the phonon bath is given by [36]:

$$\frac{\partial E_{el}}{\partial t} = 2\pi N_c N(\epsilon_F) \int_0^\infty \alpha^2 F(\omega) (\hbar\omega)^2 \left[N(\omega, T_L) - N(\omega, T_{el}) \right] d\omega \tag{4.4}$$

where N_c is the number of cells in the sample, $N(\epsilon_F)$ is the density of states of both spins per unit cell, $N(\omega, T_i)$ are the Bose-Einstein distribution function ($i = L$, el) and $\alpha^2 F(\omega)$ is the electron-phonon spectral function. Equation 4.4 is the starting point to derive the temperature relaxation rate in two different limits. In the first case the high temperature approximation is considered, that is when both T_{el} and T_L are much higher than the phonon energy, while in

the second case, the phonon spectrum $F(\omega)$ is approximated by the Einstein model, therefore only one phonon mode is taken into account. In the latter case the system of coupled differential equation describing the rate equation of the electronic and the lattice temperature is:

$$\begin{cases} \dfrac{\partial T_{el}}{\partial t} = \dfrac{3\,\lambda}{\pi\hbar k_B^2}\,\dfrac{\hbar^3\Omega_0^3}{T_{el}}\,\left[N(\Omega_0,T_L) - N(\Omega_0,T_{el})\right] + \dfrac{p}{C_{el}} \\ \dfrac{\partial T_L}{\partial t} = -\,\dfrac{3\,\lambda}{\pi\hbar k_B^2}\,\dfrac{\hbar^3\Omega_0^3}{T_{el}}\,\left[N(\Omega_0,T_L) - N(\Omega_0,T_{el})\right]\,\dfrac{C_{el}}{C_L} \end{cases} \tag{4.5}$$

In equation 4.5, λ is the electron-phonon coupling constant, which can be expressed as the second moment of the Eliashberg's function $\alpha^2F(\omega)$, $\lambda\langle\omega^2\rangle = 2\int_0^\infty(\alpha^2F(\omega)\omega)d\omega$. $\hbar\Omega_0$ represents the energy of the Einstein mode to which the phonon spectrum is approximated and k_B represents the Boltzmann's constant. $N(\Omega_0,T_L)$ and $N(\Omega_0,T_{el})$ are the Bose-Einstein distributions at the phonon frequency and at the lattice and the electronic temperature, respectively. Other important parameters in equations 4.5 are the lattice specific heat C_L and the electronic specific heat $C_{el} = \gamma_{el}\,T_{el}$, where γ_{el} is the linear coefficient of the specific heat. Finally, p represents the absorbed power density. Both the specific heats and p are expressed per unit of volume.

By fitting the T_{el} solution of the system of rate equations to the experimentally determined $T^*_{el}(t)$, it is possible to extract a value for the the electron-phonon coupling constant λ.

4.5.2 The Two Temperatures Model on BiTeI

In Section 4.3.1 we extracted the temporal evolution of the effective electronic temperature through the EDCs analysis. The 2TM provides us with a method to relate the experimentally measured relaxation time τ_T of the temporal evolution of $T^*_{el}(t)$ to λ. However, the 2TM predicts a relaxation rate which is essentially fluence-independent [38], while we observe a fluence-dependent relaxation rate, as it can be argued by the trend reported in Figure 4.7. In order to gain information from the 2TM, an assumption is made. Namely, we chose to consider as relevant for the extraction of the λ through the 2TM only the measurement done at the lowest fluence (note that the model described by equations 4.5 is indeed valid in this situation). We motivate this choice with the hypothesis that the fleunce-dependence of the relaxation time originates from an additional mechanism that introduces a bottleneck in the relaxation dynamics, which depends on the fluence and thus it is negligible at low fluence. It cannot be an additional scattering channel, since the relaxation time increases with the fluence. It seems a reasonable assumption that a bottleneck effect is less relevant at low fluence, since the quasiequilibrium between electrons and a bosonic population is less effective at low excitation densities. Our hypothesis is that, by considering the dataset taken at the lowest fluence, the relaxation time we consider, and from which we extract the electron-phonon coupling, is due solely to electron-phonon scattering processes.

Our procedure consists in a numerical solution of the 2TM rate equations system, which is then fitted to the experimental data. The physical quantities appearing in equations 4.5 must be determined with precision in order to obtain reliable results. We thus made careful estimates (explained in the following paragraphs) for the values of Ω_0, C_L and p, leaving us with only two free fitting parameters: the electronic specific heat and the electron-phonon coupling constant λ.

We took the mean phonon frequency from the experimental phonon spectra of BiTeI as measured by Sklyadneva *et al.* using Raman spectroscopy [39]. The main Raman active mode that they observed is centred at $99\,\mathrm{cm}^{-1}$, which corresponds to $\sim 12\,\mathrm{meV}$. This value was compatible with the main frequency that they obtained through the calculation of the phonon dispersion using the density-functional perturbation theory in a mixed-basis pseudopotential approach. Therefore, our analysis considered the Ω_0 equal to this phonon frequency.

Concerning the lattice specific heat we considered the limit $T_L \gg T_{Debye}$ (this is indeed true for $T_L \geq 100\,\mathrm{K}$). In such limit, the specific heat of the lattice is proportional to n, the ions density per unit volume: $C_L = 3k_B\, n$ [37]. To determine n we divided the number of the ions in a primitive cell of BiTeI by the volume of the primitive cell calculated using the lattice constants shown in Figure 2.3 (c). The resulting value of the lattice specific heat is equal to $C_L = 0.99\,\mathrm{J/(K\ cm^3)}$.

Finally, we calculated the power energy density deposited in the system by the pump pulse. This is defined as the energy absorbed by the system per unit of volume and time (measured in $[\mathrm{J/(s\ cm^3)}]$).

4.5.2.1 Modelling the absorbed power density

The power density can be express as [40]:

$$p(t) = \frac{P_0}{V}\,\frac{2\sqrt{ln2}}{\sqrt{\pi}}\,e^{-4ln2\frac{t^2}{\varsigma^2}} \tag{4.6}$$

In equation 4.6, P_0 represents the pump pulse mean power absorbed by the sample and it is divided by the sample volume V in which the energy is deposited. ς represents the pulse temporal FWHM, obtained, for example, by auto- or cross-correlation measurements.

Since the temporal duration of both pulse and probe pulse was already determined (60 fs and 330 fs respectively), only P_0 and volume V are unknown in equation 4.6.

In determining P_0, we have to take into account the gaussian profile of the pump and probe pulses [40]. The common procedure to determine the fluence is based on the assumption of an uniform energy distribution in the pulse section (a disk with diameter equal to the FWHM). However, the lateral profile of the pulses is gaussian, so a gaussian power distribution for both the pump and

probe pulses must be considered. This results in the fact that the measured signal (related to the gaussian case) is originated by an effective fluence, which is always smaller than the one calculated in the homogeneous case. The two values are related by a term that depends on the relative size of the pump and probe pulses. In our measurements the value of the pump power (that we measured with a power meter placed on the pump optical path) had to be multiplied by the factor $0.5 \ln 2 \sim 0.34$.

To obtain the mean power absorbed by the sample, two additional steps became necessary: the first was to take into account the geometry of our experimental set-up and the second step was to take into consideration the absorption coefficient of the material at the pump wavelength (800 nm) and at the specific angle of incidence (45°). With regard to the former, the pump beam illuminated the sample forming an angle of 45° with respect to the normal to the surface, therefore the power had to be divided by a factor $\sqrt{2}$.

Taking into account the aspects mentioned above, we calculated the absorbed power P_0 by using the following expression:

$$P_0 = P_{pump} \cdot 0.34 \cdot \frac{1}{\sqrt{2}} \cdot [1 - R(45°, 800\,\text{nm})] \tag{4.7}$$

where $R(45°, 800\,\text{nm})$ is the reflectivity of BiTeI for a radiation having a wavelength of 800 nm incident at 45° with respect to the sample normal. We measured $R(45°, 800\,\text{nm})$ in $p-$polarization (the polarization of our pump pulse) and it results equal to 0.227.

The volume in which the pump energy is deposited is usually approximated as a cylinder whose top area is a circle of diameter equal to the spatial FWHM of the pump pulse (experimentally determined), and whose height is the penetration depth d:

$$V = \pi \frac{(\text{FWHM})^2}{4} d = \pi \frac{(\text{FWHM})^2}{4} \alpha^{-1} \tag{4.8}$$

The penetration depth is equal to the inverse of the absorption coefficient α of the sample that is related to the imaginary part of the complex refractive index $\widetilde{n} = n + i\kappa$ of the material:

$$\alpha = \frac{4\pi\kappa h\nu}{hc} \tag{4.9}$$

where $h\nu$ is the energy of the radiation (in our situation, $h\nu = 1.55\,\text{eV}$, the pump energy).

Since it is not reported in the literature, we had to measure the complex refraction index $\widetilde{n}$, in order to obtain the penetration depth for calculating the volume V. Such value was determined through a reflectivity measurement on the BiTeI sample for both $s-$ and $p-$ polarizations. This has been done by fitting the (complex) Fresnel equations for absorbing materials to the experimental data (reported in Figure 4.11).

The experimental data were acquired by illuminating the BiTeI sample with a 800 nm beam and measuring the power of the reflected beam as a function of

the incidence angle varied from 5° to 75°. By dividing the power of the reflected beam with the power of the incident beam, we obtained the reflectivity value needed. We repeated the same measurement for both $s-$ and $p-$ polarizations, collecting the data shown in Table 4.5.

Table 4.5: Values of the reflectivity for BiTeI at 800 nm as a function of the incidence angle. The values for both $s-$ and $p-$ polarization are reported.

	Reflectivity	
Angle of incidence (°)	R_s	R_p
5	0.325	0.330
10	0.330	0.335
20	0.359	0.315
30	0.365	0.286
40	0.399	0.247
45	0.423	0.227
50	0.438	0.202
60	0.493	0.138
65	0.552	0.103
70	0.596	0.071
75	0.548	0.039

The reflectivity data were fitted by using the Fresnel equations for both the polarizations of the incident light. The Fresnel equations are derived from Maxwell's equations and describe the behaviour of light when it passes between two media with different refractive indexes. In particular, by imposing the boundary conditions at the interface between the two materials (for both the electric and magnetic fields), the equations provide the reflectivity and the transmission coefficient for both polarizations.

If the air refractive index is $n_A = 1$ and the complex refractive index of the solid equal to $\widetilde{n} = n + i\kappa$, the reflectivity for the two different polarizations can be expressed by the following equations, which are functions of the complex refraction index $\widetilde{n}$ and of the angle of incidence θ_i:

$$\begin{aligned} R_s &= \frac{(n - \cos\theta_i)^2 + \kappa^2}{(n + \cos\theta_i)^2 + \kappa^2} \\ R_p &= \frac{(n - \sec\theta_i)^2 + \kappa^2}{(n + \sec\theta_i)^2 + \kappa^2} \end{aligned} \tag{4.10}$$

Equations 4.10 are simultaneously fitted (GlobalFit routine by IgorPro) to the experimental reflectivity for both $s-$ and $p-$ polarizations (presented in Table 4.5). The result of the fit is reported in Figure 4.11. The values we

obtained are:

$$n = 1.91 \qquad \kappa = 2.92 \tag{4.11}$$

By using the value of κ, the absorption coefficient of BiTeI was calculated along with the corresponding penetration depth d, taking into account a pump wavelength of 800 nm and adopting equation 4.9. The values obtained are:

$$\alpha = 4.59 \cdot 10^5\,\mathrm{cm}^{-1} \qquad d = 22\,\mathrm{nm} \tag{4.12}$$

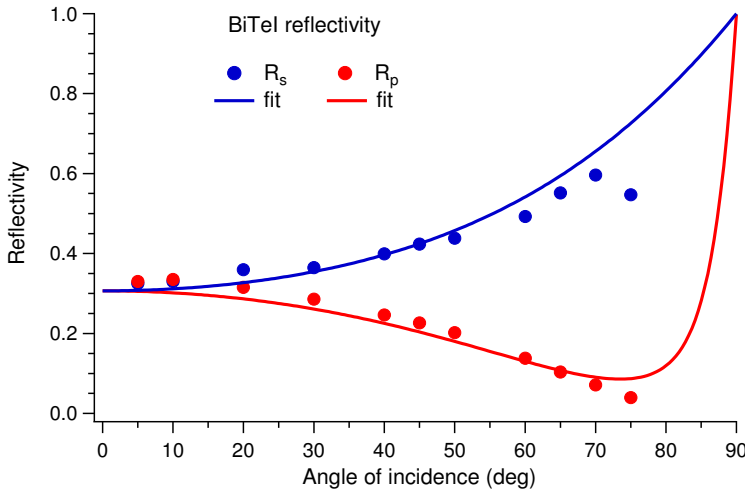


Figure 4.11: Reflectivity measurements on BiTeI at 800 nm for $s-$ and $p-$ polarizations. The solid lines represent the global fit obtained through Fresnel equations for lossy materials. The fit provides the values of the real and imaginary parts of the BiTeI complex refractive index $\widetilde{n} = n + i\kappa$, respectively equal to $n = 1.91$ and $\kappa = 2.92$.

4.5.2.2 Electron-Phonon coupling constant in BiTeI

The coupled differential equations 4.5 were used to fit the data of the temporal evolution of T^*_{el} obtained from the experiment at lowest fluence. The coefficient of the linear electronic specific heat, defined by the expression $C_{el} = \gamma_{el}\, T_{el}$, and the electron-phonon coupling constant were the only free parameters of the fit. Table 4.6 reports the values of the other parameters appearing in equations 4.5 that were kept fixed during the fitting procedure.

Table 4.6: Parameters considered in the Two Temperatures Model.

Parameter	Value
Phonon energy $\hbar\Omega_0$ [eV]	0.012
Lattice specific heat C_L [J/(K cm^3)]	0.99
Pulse temporal FWHM ς [ps]	0.33
Energy density $\frac{P_0}{V}$ [J/(s cm^3)]	7.8
Base system temperature [K]	100

Figure 4.12 shows the temporal evolution of the electronic and the lattice temperatures, as obtained from the fit (the residual between T^*_{el} and the fit is reported in the upper panel). We observed that, after 8 ps, the electrons have almost completely transferred their extra energy to the lattice via the electron-phonon interaction.

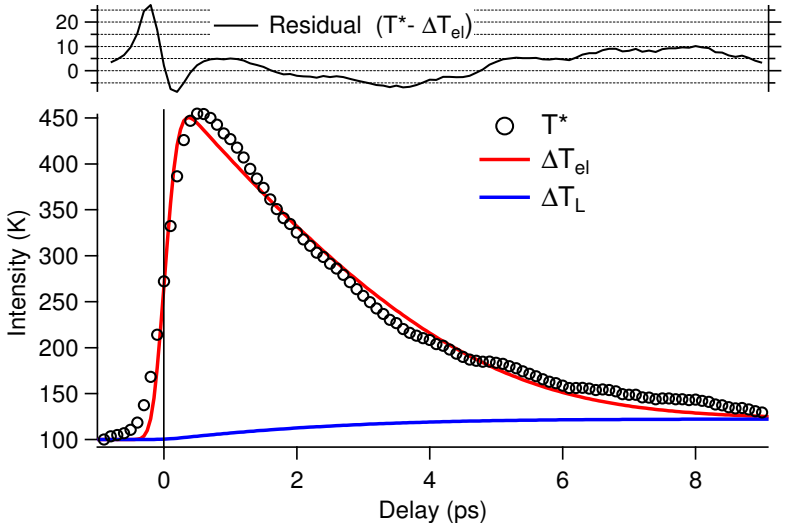


Figure 4.12: Temporal evolution of the electronic temperature and the lattice temperature (red and blue lines respectively), as obtained from the fit of the 2TM to T^*_{el} from the experiment at lowest fluence (experiment A). The solid black line in the upper panel represents the residual. The fitting procedure returns a value of the electron-phonon coupling constant of the spin-split states of BiTeI equal to $\lambda = 0.039$.

From the result of the fit we obtained the values of the two free parameters (the coefficient of the linear electronic specific heat and the electron-phonon

coupling):

$$\gamma_{el} = (7.4 \pm 0.2) \cdot 10^{-5}\,\mathrm{J/(K^2 cm^3)} \tag{4.13}$$

$$\lambda = 0.039 \pm 0.001 \tag{4.14}$$

The obtained λ implies that the electron-phonon interaction is very weak in the surface spin-split states of BiTeI. Furthermore, the value of λ is comparable to the electron-phonon coupling constant recently reported for the topological surface state of Bi_2Se_3 and Bi_2Te_3 [41].

We stress the fact that λ has been extracted with the assumption that the relaxation time characterizing the electronic temperature is solely due to the electron-phonon scattering processes. Further analysis on temporal evolution of T_{el}^{*} at different fluences should be done introducing a modification of the 2TM equations in order to take into account the fluence-dependent slowdown in the relaxation of the electronic temperature.

Chapter 5

Dichroic ARPES on BiTeX

The term Circular Dichroism (CD) refers in general to the phenomena in which the system has a different response to probing photons with left and right circular polarizations (LCP and RCP respectively). If the propagation direction of the light is assumed to point out of the plane, the LCP (RCP) is defined as the counter-clockwise (clockwise) rotation. In these cases the photons are characterized by negative (positive) helicity.

In particular, in PES experiments the dichroic signal is measured as the difference in the photoemission intensity obtained with the two opposite helicities. Recently, the circular dichroic ARPES (CD-ARPES) has been proposed as a tool to study the strongly spin-orbit coupled materials, in which the helicity of the incident light can couple to the electronic spin degree of freedom through the total angular momentum.

The first part of this chapter illustrates the most recent CD-ARPES applications to the study of topological insulators Bi_2Se_3 [42, 43] and Bi_2Te_3 [44]. In particular, we focus on the different physical interpretations of the origin of this dichroic signal. The second part of the chapter presents the CD-ARPES measurements we performed on the BiTeX semiconductor family: we analyse the Fermi surface of BiTeI and the dependence of the CD signal on the incoming photon energy. Finally, we discuss our results and we try to elucidate the possible future development of this technique, and possible further investigation on this interesting family of compounds.

5.1 Physical interpretation of the CD-ARPES in strong spin-orbit coupled systems

The photoemission process described by the matrix element of equation 3.9 is based on an optical transition. In general, but it becomes particularly critical in the case of a strong spin-orbit coupled system, the final state of the optical

transition can be expanded over a set of eigenstates with different values of the total angular momentum **J** (and J is its eigenvalue). The partial transition to the various contribution of the the final state is reflected in the matrix element and, as a consequence, in the photoemission intensity. Circularly polarized light produces optical transitions towards final states with different value of J depending on the photons helicity ($\Delta J = +1$ with RCP light and $\Delta J = -1$ with LCP light). As a result, the photoemission intensities obtained by using LCP and RCP photons are different and a dichroic signal can be observed. This description of the CD-ARPES dichroism clearly requires taking into account the photoemission process in a one-step model, which is often a difficult task from a computational and theoretical point of view. Therefore, some approximated models have been developed recently focusing only on the initial state, with the aim to extract directly an information on J and on the spin polarization.

Hereafter we describe the first CD-ARPES studies of the spin-polarized surface states of topological insulators Bi_2Se_3 [42, 43] and Bi_2Te_3 [44] (but similar analysis has been carried out on others Rashba system [45, 46]), and we briefly introduce the question of the final state effect, of mandatory importance for the understanding of our experimental results.

Different properties of the initial state have been proposed to originate the dichroism in the surface states of the topological insulators Bi_2Se_3 and Bi_2Te_3. Park *et al.*, in particular, investigated the dichroism in Bi_2Se_3 using by circularly polarized light [42]. Figure 5.1 (d) shows the surface state with two different colors corresponding to the opposite signs (red is associated to $-$, blue to $+$) of the dichroic signal $I^{RCP} - I^{LCP}$. This dichroism is evident in Figures 5.1 (a)-(c) that illustrates the Fermi surface maps for the two different polarizations as well as their difference. Figure 5.1 (e) displays the CD intensity as a function of the azimuthal angle as extracted from MDCs at binding energies equal to 50 meV and 350 meV (dashed lines in Figure 5.1 (d)).

The authors attributed the measured CD to the existence of a strong local orbital-angular momentum in the surface states and this hypothesis was supported by first-principles calculations predicting a large expectation value of the angular momentum operator. Since the surface states of topological insulators are spin polarized and a strong spin-orbit coupling is present, information on the expectation value of the spin degree of freedom can be deducted from the value of L. An electron in a $p-$state is excited by a circularly polarized photon in finale states having mainly $d-$ or $s-$character, according to the dipole selection rules, and the occurring optical transitions is different depending of the helicity of the incident light. In the model of Park and coauthors, the difference in the electric dipole matrix element is directly reflected in the CD signal, which results roughly proportional to the scalar product between the direction of the orbital-angular momentum and the direction of incoming photons [47].

A different interpretation, for a similar CD-ARPES experiment on Bi_2Se_3, was proposed by Wang *et al.* without the necessity to introduce a local angular momentum, by simply considering the spin degree of freedom [43]. In particular the authors developed a quantitative relationship between the spin polarization

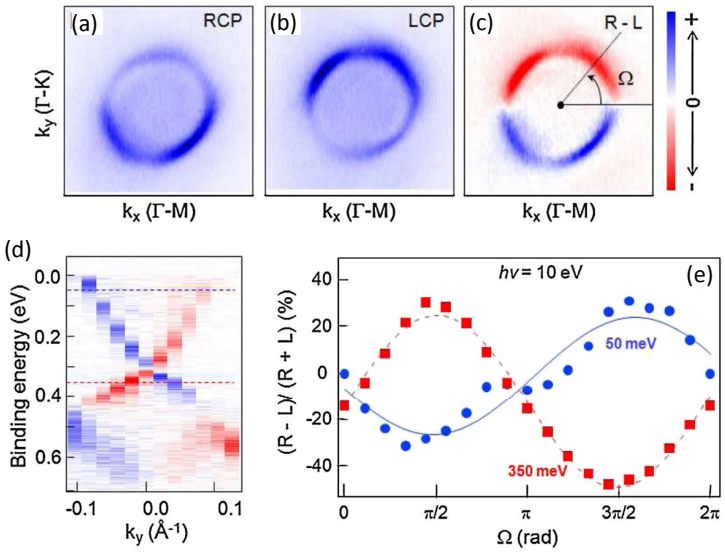


Figure 5.1: (a)-(c) Fermi surface maps of Bi_2Se_3 obtained by ARPES measurement with RCP and LCP photons at $h\nu = 13\,\text{eV}$, as well as their difference (RCP-LCP) [42]; (d) CD-ARPES map along the $k_y = 0$ direction [42]; (e) circular dichroic intensity as a function of the azimuthal angle Ω at the binding energies equal to 50 meV (blue circles) and 350 meV (red squares) [42].

of the initial state and the circular dichroic intensity. They considered the following Hamiltonian for a system with spin-orbit coupling:

$$H = \frac{\mathbf{P}^2}{2m} + V(\mathbf{r}) + \frac{\hbar}{4m^2c^2}\left(\mathbf{P} \times \nabla V\right) \cdot \mathbf{s} \tag{5.1}$$

where $\mathbf{P}$ is the momentum operator, $\mathbf{s}$ is the electron spin and $V(\mathbf{r})$ is the crystal potential. The coupling to the external electromagnetic field is included into the model through the photon vector potential $\mathbf{A}$, $\mathbf{P} \rightarrow \mathbf{P} - e\mathbf{A}$. The photoemission matrix element between the initial and final states results equal to:

$$M(\mathbf{k}, f) = \langle f_k | \mathcal{P} \cdot \mathcal{A} | \mathbf{k} \rangle \tag{5.2}$$

where $\mathcal{A}$ is the Fourier transform of $\mathbf{A}$ and $\mathcal{P}$ is defined as $\mathcal{P} = \frac{e}{m}\mathbf{P} - \frac{e\hbar}{4m^2c^2}\left(\nabla V \times \mathbf{s}\right)$. Starting from equation 5.2, the authors extracted the expression of the photoemission intensity by considering circularly polarized light and by exploiting time-reversal and crystal symmetries. They obtained an expression for the circular dichroism equal to:

$$\Delta I = a^2\, \mathcal{I}m(\mathcal{A}_x \mathcal{A}^*{}_y)\, \langle S_z \rangle_k - 4ab\, \mathcal{I}m(\mathcal{A}_z \mathcal{A}^*{}_y)\, \langle S_x \rangle_k \tag{5.3}$$

where a and b are bandstructure dependent complex constants. The intensity of the dichroic signal is a function of the spin polarization of the initial

state. Furthermore, by considering the time-reversal symmetry and the three-fold rotational symmetry, the authors proposed a method to deduce the three spin components of the initial state by taking the difference or the sum of the dichroic signal in different experimental geometry.

The possibility to exploit CD-ARPES to directly investigate the spin of the initial state, neglecting completely the final state effects, has been very recently questioned by measurements at variable photon energies. Sholz *et al.* investigated the circular dichroism in the surface state of a different topological insulator, Bi_2Te_3 [48]. In contrast to the aforementioned studies on Bi_2Se_3, the authors performed CD-ARPES measurements at various photon energies between 20 eV and 100 eV [48]. Figure 5.2 displays the modulation of the CD signal. Interestingly, the sign of the dichroism changes between the selected photon energies (21 eV, 25 eV, 55 eV and 100 eV) above as well as below the Dirac point. This behaviour cannot be interpreted as a change neither of the spin polarization [43] nor of the orbital angular momentum of the initial state [44]. No simple physical effect, in fact, can account for such a dependence of these initial state properties on the incident photon energy. Sholz and coworkers interpreted the change in dichroism as the result of final state effects in the photoemission process. This hypothesis is sustained by first principle calculations based on the one-step model, which includes matrix element's effect, multiple scattering effects in both the initial and the final states and the change in the photoelectron escape depth. The calculations qualitatively reproduced the change of the CD sign supporting its interpretation in terms of final states effects. More specifically, the authors attributed the energy dependence of CD to the optical transition from the p-like topological surface states to final states with different d-like character. The $p \rightarrow d$ optical transitions are favorable in the dipole approximation, hence, in the case of circularly polarized light, LCP photons ($\Delta J = -1$) can excite specific transition, not accessible with RCP photons ($\Delta J = +1$) and viceversa, thus resulting in a large change in the photoemission intensity. This large asymmetry in the PES signal associated to the different optical transitions is proposed to determine the experimental changes in the dichroic signal.

Furthermore, besides the problem of the physical origin of the CD effect, another important question remains unresolved in strongly spin-orbit coupled system such as topological insulators and BiTeX, i.e. the absolute value of the surface state spin polarization. In topological insulators, in particular, spin resolved ARPES experiments reported a large variation of the spin polarization, from 20% [49] to more than 85% [50, 51]. Recently, Zhu *et al.* reported density functional slab-calculations showing that the spin polarization in Bi_2Se_3 changes with the atomic layer [52]. Figures 5.3 (a)-(b) display the asymmetry in the ARPES intensity between $\pm\mathbf{k}_{\parallel}$ in the surface state of Bi_2Se_3 measured with σ and π linearly polarized light. The authors proposed that PES signal results affected by the interference between photoelectrons emitted from different atomic layers, which are characterized by different spin-orbit texture and which gain a phase factor owing to the different distance travelled between the various

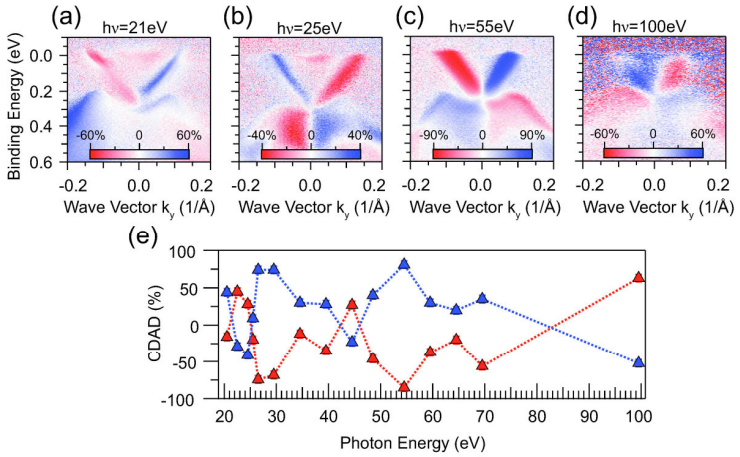


Figure 5.2: (a)-(d) CD-ARPES maps of the surface state of Bi_2Te_3 at four selected photon energies (21 eV, 25 eV, 55 eV and 100 eV, respectively). Clearly, the circular dichroism changes both the intensity and the sign as a function of the photon energy [48]; (e) dichroism asymmetry evaluated 100 meV above the Dirac point as a function of the photon energy [48].

layers:

$$I \propto \sum_{\sigma} \left| \sum_{i} e^{-ik_z z_i} \langle e^{i\mathbf{k}_{\parallel}\cdot\mathbf{r}_{\parallel}} | \mathbf{A}\cdot\mathbf{p} | \alpha_i \psi^{\sigma}_{i,\mathbf{k}_{\parallel}} \rangle \right|^2 \tag{5.4}$$

where the topological surface state is expressed as a linear combination of the layer-dependent eigenstates, $\Psi_{TTS} = \sum_{i,\sigma} \alpha_i \psi^{\sigma}_{i,\mathbf{k}_{\parallel}}$, whit i and σ being layer and spin indexes. This interpretation is supported by the good agreement between the calculated and the experimental band structure. Figures 5.3(c)-(f) present the projections of the p orbitals for the top-most atomic layers on the various L component. The strongly layer-dependent orbital polarization is reflected into the spin polarization via the SO interaction, resulting in an entangled spin-orbital texture of the surface states that depends on the atomic layer. Interestingly, in this model also the calculated spin polarization is influenced by the photoelectron interference and its dependence on the photon energy, the incoming light polarization and the angle of incidence can explain the aforementioned large variation in the measured spin polarization intensity in the surface states of the topological insulators in various experiments.

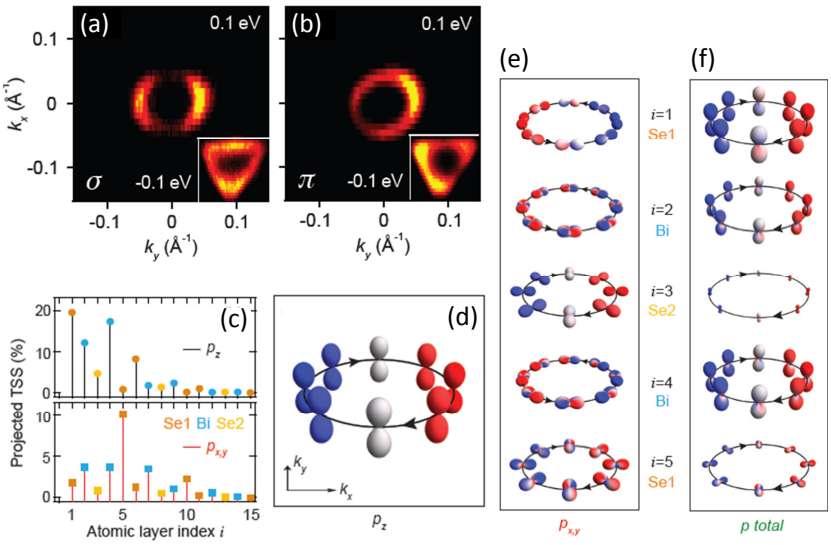


Figure 5.3: (a)-(b) constant energy ARPES maps at 0.1 eV above the Dirac point (and 0.1 eV below E_F in the insets) obtained with π and σ linearly polarized light respectively [52]; (c) percentage contribution of the p orbitals to the topological surface state for the top 15 atomic layers [52]; (d)-(f) orbital-projected charge density along the $k-$contour at 0.15 eV above the Dirac cone [52]. The p_z projection is independent from the atomic layer, while the layer-dependency is strong for the in-plane projection, resulting in a total spin-orbit texture of the topological surface state that varies with the atomic layer.

5.2 Circular dichroic ARPES measurements on BiTeX

We investigated the circular dichroism in BiTeX family (with X= I, Br, Cl) using CD-ARPES at variable photon energies. The CD signal was obtained as the difference between the photoemission intensities collected for the two photon helicities, whereas the normalized CD-signal is obtained by dividing by the total measured intensity,

$$\text{Normalized CD} = \frac{I^{LCP} - I^{RCP}}{I^{LCP} + I^{RCP}} \tag{5.5}$$

5.2.1 Measurement conditions

The CD-ARPES experiment was performed at the APE beamline at Elettra synchrotron in Trieste. The experimental endstation is equipped with an hemi-

spherical Scienta SES2002 electron spectrometer with energy and angular resolution set respectively equal to 20 meV and 0.3°. The samples were cleaved *in situ* at a base pressure of $p \sim 2 \cdot 10^{-10}$ mbar and kept at low temperature (approximately 80 K) using a LN_2 cryostat. The UV light impinging on the sample surface was generated by an APPLE II ondulator, capable to deliver circularly polarized in the range between 20 eV and 50 eV.

Additional CD-ARPES mesurements were performed on BiTeI at the BACH beamline at Elettra in order to exploit higher photon energies (from 70 eV to 200 eV). The pressure was $p \sim 3 \cdot 10^{-10}$ mbar, the temperature was approximately 80 K and the photoelectrons were collected and analysed by a Scienta R3000 electron spectrometer, with energy and angular resolution set equal to 20 meV and 0.25°.

5.2.2 Dichroic constant energy mapping of BiTeI

We start considering the constant energy map (CEMs) of BiTeI measured with circularly polarized light at 40 eV. The contours of the spin-split surface states are shown in Figure 5.4 for four selected binding energies (0 meV, 100 meV, 200 meV and 280 meV respectively). At binding energy equal to 0 meV, that corresponds to the Fermi level, the CE map clearly displays two distinct and concentric contributions (outer and inner sheets) characteristic of the Rashba-type spin splitting. The outer branch has six-fold symmetry with a three-fold intensity modulation. By increasing the binding energy, the contours of both the outer and the inner sheets shrink towards the center of the Brillouin zone, thus clearly indicating an electron like dispersion with positive effective mass.

The dichroic CEMs for the same binding energies are displayed on the right side of Figure 5.4. The inner contour presents a two-fold symmetry in the dichroic signal, whereas the outer contour shows six pockets of intensity centered at the corners of the six-fold Fermi surface, with three-fold symmetry and alternating dichroic signal.

This behaviour is suggestive of a simple interpretation in term of different cartesian components of the spin polarization. In the specific, the three-fold modulation in intensity well resembles the $z-$component of the spin polarization (perpendicular to the surface plane) [53]. The appealing possibility to still exploit CD-ARPES to gain an insight in the spin polarization motivated our detailed study of the dichroism dependence on the photon energy. In the next paragraphs we discuss our efforts to disentangle the interesting physical information about the initial state from the existing final state effects.

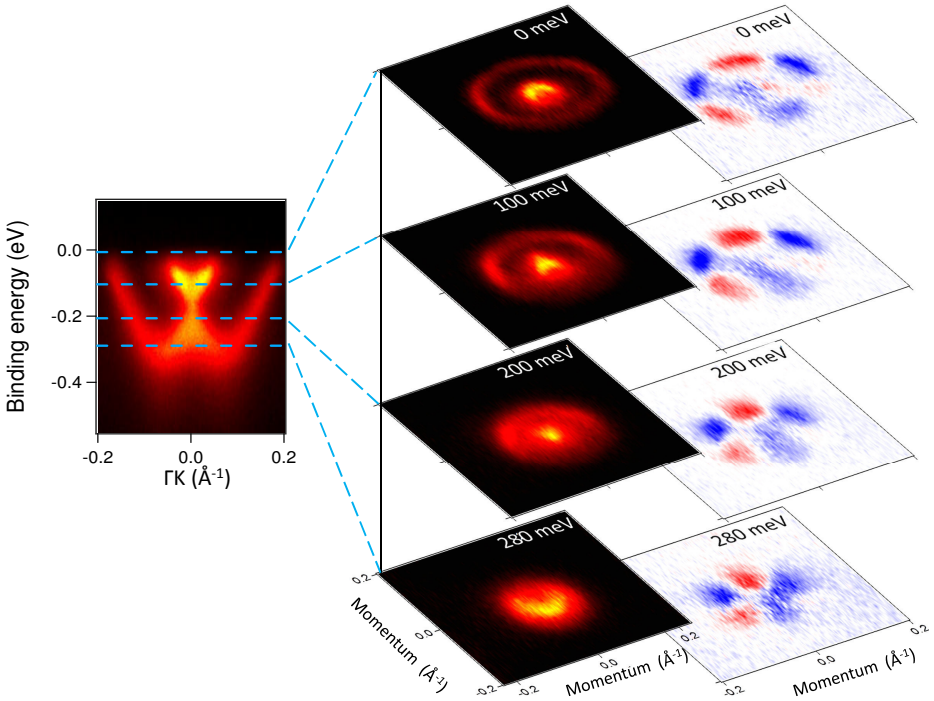


Figure 5.4: Constant energy maps of BiTeI at $h\nu = 40\,\text{eV}$ for four selected binding energies (0 meV, 100 meV, 200 meV and 280 meV respectively) and the corresponding dichroic signal (on the right side). The constant energy contour at E_F clearly shows two Fermi sheets characterizing the Rashba-type spin splitting. The dichroic signal of the outer contour presents six pockets with three-fold symmetry and alternating sign of the dichroism.

5.2.3 Energy evolution of dichroism in BiTeX

We performed CD-ARPES experiments on all the compounds of BiTeX family along the $\overline{\Gamma K}$ high symmetry direction. All the systems exhibit dichroism in the spin-split bulk valence band and in the spin-split surface states, as shown in Figure 5.5, for example, in the case of BiTeCl at a photon energy equal to 25 eV. We focused on the spin-split surface states by analysing the dependence of the circular dichroic signal on the the incoming photon energy.

BiTeI. Figures 5.6 (a)-(d) show the ARPES maps of BiTeI and the corresponding dichroic signals obtained along the $\overline{\Gamma K}$ direction with a photon energy equal to 25 eV and 48 eV. Both the spin-split surface and the bulk conduction band states are visible at 48 eV, while at 25 eV only the surface states, with the largest binding energy, are clearly resolved. By comparing Figure 5.6 (c)-(d) we noticed that the dichroism is strongly different at the two selected photon

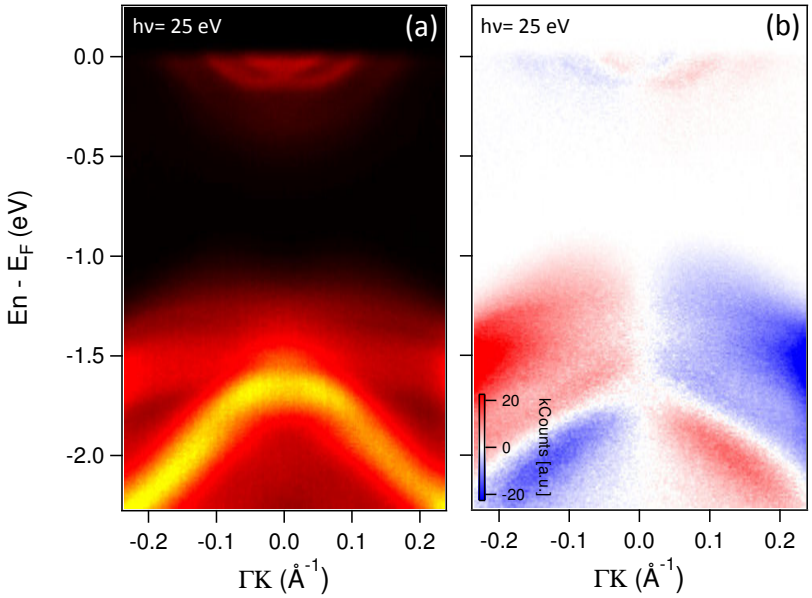


Figure 5.5: CD-ARPES image of BiTeCl performed along $\overline{\Gamma K}$ with the photon energy equal to 25 eV: (a) band dispersion obtained with horizontal polarization; (b) circular dichroic ARPES map as result from the difference between the photoemission intensity with LCP and RCP. Both the valence band and the surface spin-split states exhibits dichroism.

energies. In fact, at 25 eV only one change in sign of CD occurs at the $\overline{\Gamma}$ point, while the CD-ARPES map at 48 eV presents several nodal points where CD changes sign. The variations of CD exhibited by the spin-split states are even more evident in Figure 5.6 (e), which illustrates the behaviour of the circular dichroism of BiTeI at photon energies between 25 eV and 100 eV. Interestingly, at 100 eV the CD characterizing the outer branches of the two parabolas changes sign.

We integrated the CD intensity over a small energy window at the Fermi level in order to obtain a quantitative estimation of the dichroism asymmetry characterizing the different states. Figure 5.6 (f) shows the normalized CD at the Fermi level as a function of the wave vector for three selected photon energies (25 eV, 48 eV and 100 eV). The different behaviour of dichroism at the three different photon energies is remarked by the difference in the number of nodal points in the CD intensity, respectively 1, 3 and 5.

BiTeCl and BiTeBr. The BiTeCl and BiTeBr band dispersions measured along $\overline{\Gamma K}$ at 25 eV photon energy (as similarly displayed for BiTeI in Figures 5.6 (a)) are shown in Figure 5.7 (a)-(b).

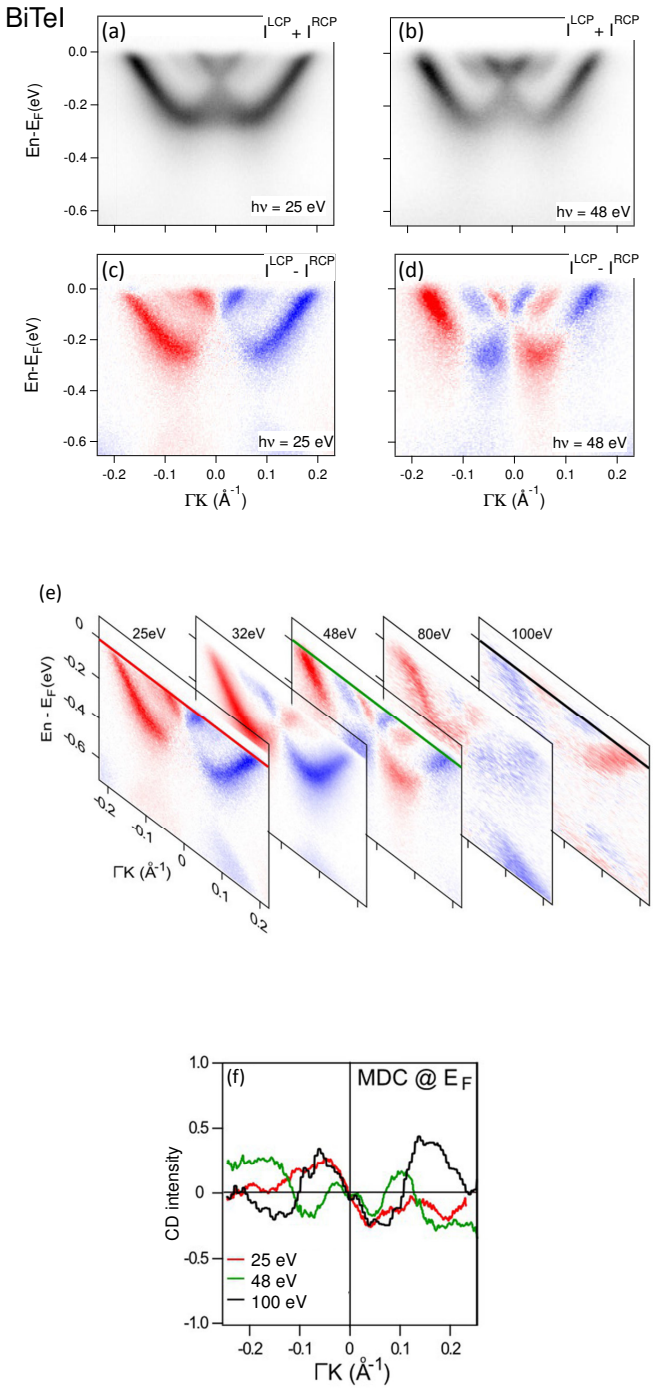


Figure 5.6: Circular dichroic ARPES on BiTeI: (a)-(b) band dispersion along $\overline{\Gamma K}$ direction with the photon energy equal to 25 eV and 48 eV and the corresponding dichroic signal (c)-(d); (e) circular dichroism when varying the incoming photon energy between 25 eV and 100 eV; (f) normalized dichroic signal as a function of the electron momentum at the Fermi level for three selected photon energy, 25 eV, 48 eV and 100 eV respectively.

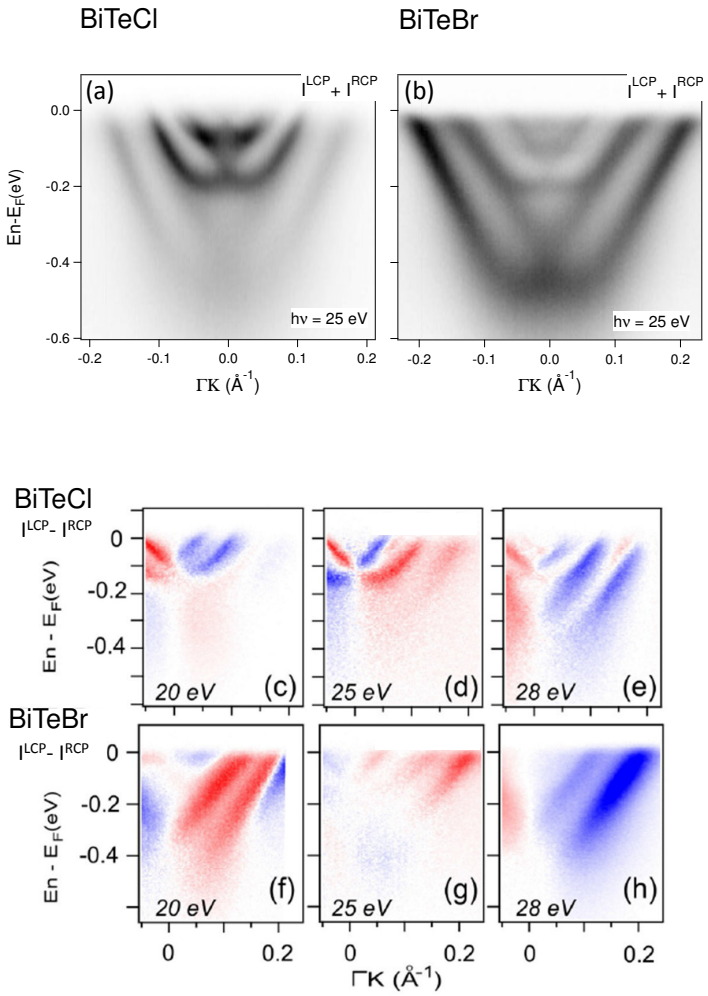


Figure 5.7: Circular dichroic ARPES in BiTeCl and in BiTeBr: (a)-(b) band dispersion measured along $\overline{\Gamma K}$ direction with a photon energy equal to 25 eV of BiTeCl and BiTeBr respectively; (c)-(e) circular dichroism of BiTeCl for positive wave vector at three selected photon energies (20 eV, 25 eV and 28 eV) and the same for BiTeBr (f)-(h). In both systems the dichroism changes sign and intensity several times as a function of the photon energy.

The high quality of the data allows to clearly resolve three pairs of spin-split states for both the compounds, as predicted by the first-principle calculations and experimentally resolved with ultrahigh resolution laser-based ARPES [26]. A thorough inspection in the band dispersion evidences that different states in the same material exhibit strong difference in the matrix element describing the photoemission intensity. This aspect becomes even clearer in the dichroic signal that we report in Figure 5.7 (c)-(h) for positive wave vector at three different photon energies (20 eV, 25 eV and 28 eV). For both materials the intensity and sign of CD change with the incoming photon energy and the three pairs of spin-split states behave differently from each others.

We compared the dichroism in the three compounds of the BiTeX family by analysing the quantitative evolution of the normalized dichroic intensity as a function of the incoming photon energy.

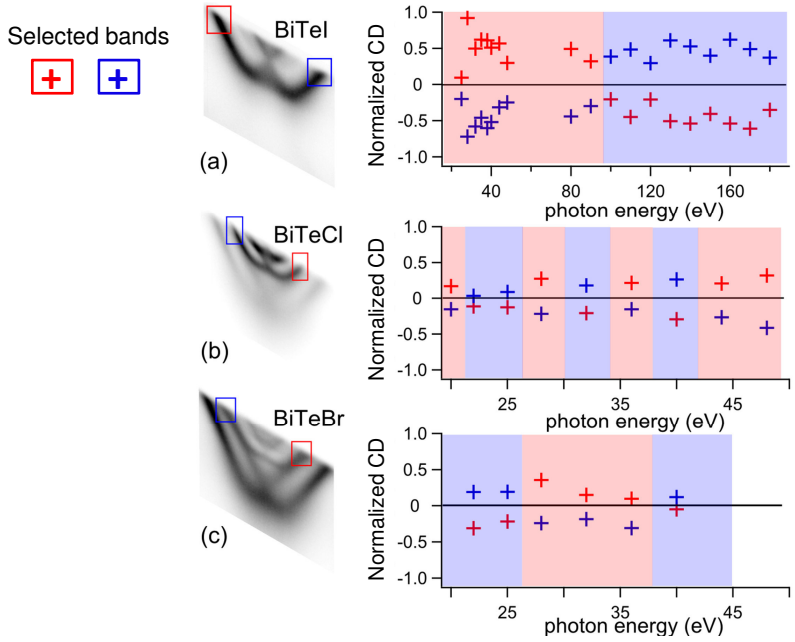


Figure 5.8: Comparison between the dichroism in the BiTeX family: normalized circular dichroic signal of the selected bands as a function of the incoming photon energy for BiTeI (a), BiTeCl (b) and BiTeBr (c). The change in color of the graph background corresponds to the change of the sign in the dichroism.

Figure 5.8 illustrates the CD signal relative to one pair of spin-split states (indicated by red and blue squares) for each material. The color of the graphs background vividly convey the changes of the CD sign. Very interestingly, we notice that the dichroism in the three materials has very different behaviour when varying the photon energy. In particular, while the selected band of BiTeI

exhibits only one change of CD sign at relatively high photon energy (100 eV), in BiTeCl several changes occur in few eV (in a range of 30 eV the CD signal changes sign six times) and in BiTeBr CD exhibits two changes of sign (25 eV-28 eV and 36 eV-40 eV). Also the intensity of the CD signal is different in the three materials: BiTeI presents a CD asymmetry approximately equal on average to 50%, except in the region of the CD sign's change, with the maximum value of almost 100% at the photon energy equal to 28 eV; instead in the other two compounds the CD intensity is less than 30% for all the photon energies considered.

5.3 Discussion and future investigations

The experimental CD-ARPES data, relative to BiTeX family presented in the previous section, show a strong dependence of the dichroism on the incoming photon energy. At first inspection, this observation suggests a strong influence of the final state effect, similarly to the case of the topological insulator Bi_2Te_3 studied by Scholz *et al.* [48]. They attributed the variation in the circular dichroic signal to final state effect involving optical transitions form the $p-$like initial states to final states with enhanced $d-$like character. However, despite of the similarity in the crystal structure and in the band dispersion, the dichroic signal in BiTeI remains almost unchanged over 80 eV while in BiTeBr the CD signal changes several times at lower photon energy. This difference suggests that the matrix element influeced by the $p \rightarrow d$ transitions cannot alone explain the peculiar behaviour of circular dichroism observed in the three compounds. Anyhow, in order to be more quantitative and in order to address the role of final state effect, calculations of the photoemission intensity using first-principle calculations based on one-step model should be performed for BiTeX compounds, as already done for Bi_2Te_3 [48].

Here we consider an alternative interpretation for the observed change in dichroism, that takes into account the layer-dependence of the spin-orbit texture of the spin-split surface states wavefunction. In fact, if the surface states have a layer-dependent multi-orbital character, the photoemission intensity is affected by the interference between photoelectrons originated from different atomic layers, as observed by Zhu *et al.* in Bi_2Se_3 [52]. Based on this argument, the change in dichroism depends on the layer-dependent spin-orbital texture of the surface states.

Figure 5.9 shows the spin polarization, from first principles calculations performed by G. Autès and Prof. O. Yazyev (at EPFL in Lausanne), along y projected on different layers for the first six atoms of the Te terminated surface of BiTeI. The size of the dots corresponds to the weight of the states on the atom, while the color represents the spin direction. The calculated projections indicate that the spin polarization is different for the three different atoms, in particular for energies close to the crossing point of the spin-split surface states. In particular, in the case of the I atom the spin projection at the bottom of

the spin-split states dispersion changes sign when passing from the first to the second layer. This result supports the idea that the key to interpret the energy dependence of the dichroic signal observed in BiTeX is the interference between photoelectrons emitted from different atomic layers, which are characterized by different spin-orbit textures, similarly to what proposed for Bi_2Se_3 by Zhu *et al.* [52].

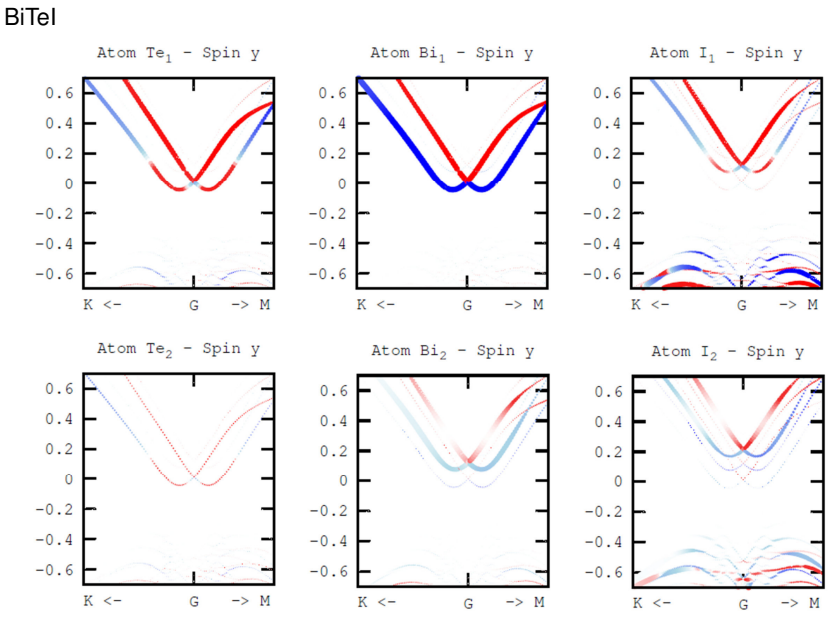


Figure 5.9: Layer-dependent spin polarization in BiTeI: first-principle calculated spin polarization along y projected on the first six atoms of the Te terminated surface. The size and the dots refers to the weight of the states on the different atoms and the color represents the spin direction. On the iodine atoms the spin projection changes sign at the bottom of the spin-split states dispersion, passing from the first to the second layer.

We stress the fact that the data presented in this chapter clearly remark that the circular dichroism cannot be considered as a direct measurement of the intrinsic spin polarization of the initial electronic state. However, if the interpretation of the photoelectrons interference is correct, information on the initial state can be extracted through a detailed analysis of the experimental data together with theoretical calculations.

Chapter 6

Conclusions

In this thesis we investigated the non-equilibrium electronic properties of the spin-split states of the bulk Rashba system BiTeI by means time-resolved ARPES.

We analysed the Energy Distribution Curves of the density of state relative to the spin-split surface states in order to extract the effective electronic temperature T_{el}^* and the effective chemical potential μ^* characterizing the *hot* electronic gas. The dynamics of T_{el}^* and μ^* were studied as a function of the pump energy adsorbed by the sample. The characteristic relaxation time of T_{el}^* exhibits a clear fluence-dependence that cannot be accounted by the electron-phonon scattering in the relaxation process. For this reason, we extracted the electron-phonon coupling constant λ in the limit of low pump fluence, in which the contributions to the fluence-dependent slowdown of the relaxation of T_{el}^* are assumed to be negligible. The resulting value of λ is small and comparable to the value of the electron-phonon constant measured in the topological insulators Bi_2Se_3 and Bi_2Te_3 [41].

Furthermore, we developed an analysis of the one-particle spectral function dynamics through the Momentum Distribution Curves, in the perspective to extract information on the microscopic scattering mechanisms affecting the lifetime of the quasiparticle. We observed that the dynamics of the FWHM (directly related to the quasiparticle lifetime) of the lorentzian describing the quasiparticle peak in the spin-split surface states results different from the one characterizing the relaxation of T_{el}^*.

Finally, in this thesis we analysed the dichroism exhibited by the spin-split surface states of the extended family BiTeX (with X = I, Cl, Br). We observed a strong dependence of the dichroic signal on the photon energy in all the three materials. This observation suggests that the circular dichroism cannot provide alone a direct information of the intrinsic spin polarization of the initial state. However, if we interpret the dichroism as an effect of the interference of photoelectrons originate from different atomic layers which are characterized by different spin-orbit texture, information on the initial state can be extracted

through detailed analysis of the experimental data together with theoretical calculations.

Bibliography

[1] E. I. Rashba. *Sov. Phys. Solid state*, vol. 2, 1960.

[2] G. Dresselhaus. Spin-orbit coupling effect in a zinc blend structures. *Phys. Rev. Lett.*, vol. 100, 1955.

[3] Y. A. Bychkov and E. I. Rashba. Properties of a 2d electron gas with lifted spectral degeneracy. *JETP Lett.*, vol. 39, 1984.

[4] S. D. Ganichev, V. V. Bel'kov, L. E. Golub, E. L. Ivchenko, P. Schneider, S. Giglberger, J. Eroms, J. De Boeck, G. Borghs, W. Wegscheider, D. Weiss and W. Prettl. Experimental Separation of Rashba and Dresselhaus Spin Splittings in Semiconductor Quantum Wells. *Phys. Rev. Lett.*, vol. 92, 2004.

[5] T. Hassenkam, S. Pedersen, K. Baklanov, A. Kristensen, C. B. Sorensen, P. E. Lindelof, F. G. Pikus and G. E. Pikus. Spin splitting and weak localization in (110) GaAs/Al_xGa_{1-x}As quantum wells. *Phys. Rev. B*, vol. 55, 1997.

[6] S. LaShell, B. A. McDougall and E. Jensen. Spin splitting of an Au(111) surface state band observed with angle resolved photoemission spectroscopy. *Phy. Rev. Lett.*, vol. 77, 1996.

[7] Y. M. Koroteev, G. Bihlmayer, J. E. Gayone, E. V. Chulkov, S. Blugel, P. M. Echenique and P. Hofmann. Strong spin-orbit splitting on Bi surfaces. *Phys. Rev. Lett.*, vol. 93, 2004.

[8] E. Rotenberg, J. W. Chung and S. D. Kevan. Spin-orbit coupling induced surface band splitting in Li/W(110) and Li/Mo(110). *Phys. Rev.Lett.*, vol. 82, 1999.

[9] A. Varykhalov, D. Marchenko, M. R. Scholz, E. D. L. Rienks, T. K. Kiim, G. Bihlmayer, J. Sanchez-Barriga and O. Rader. Ir(111) surface state with giant Rashba splitting persists under graphene in air. *Phys. Rev. Lett.*, 108, 2012.

[10] N. W. Ashcroft and N. D. Mermin. *Solid State Physics*. Saunders College, 1976.

[11] C. Kittel. *Introduction to solid state physics*. Wiley, 1971.

[12] J. J. Sakurai and J. Napolitano. *Modern Quantum Mechanics: Revised Edition*. Addison-Wesley Publishing Company, Inc., 1994.

[13] G. Nicolay, F. Reinert, S. Hufner and P. Blaha. Spin-orbit splitting of the L-gap surface state on Au(111) and Ag(111). *Phy. Rev. B*, vol. 65, 2001.

[14] L. Petersen and P. Hedegård. A simple tight-binding model of spin orbit splitting sp-derived surface sates. *Surf. Sci.*, vol. 459, 2000.

[15] J. Premper, M. Trautmann, J. Henk and P. Bruno. Spin-orbit splitting in an anisotropic two-dimensional electron gas. *Phy. Rev. B*, vol. 76, 2007.

[16] G. Bihlmayer, Y. M. Koroteev, P. M. Echenique, E. V. Chulkova and S. Blugel. The Rashba-effect at metallic surfaces. *Surf. Sci.*, vol. 600, 2006.

[17] F. Reinert, G. Nicolay, S. Schmidt, D. Ehm and S. Hufner. Direct measurements of the L-gap surface states on the (111) face of noble metals by photoelectron spectroscopy. *Phys. Rev. B*, vol. 63, 2001.

[18] A. Tamai, W. Meevasana, P. D. C. King, C. W. Nicholson, A. de la Torre, E. Rozbicki and F. Baumberger. Spin-orbit splitting of the Shockley surface states on Cu(111). *Phys. Rev. B*, vol. 87, 2013.

[19] R. J. Elliott. Spin-orbit Coupling in Band Theory-Character Tables for Some "Double" Space Group. *Phy. Rev.*, vol. 96, 1954.

[20] S. Webbe. Crystallography Picture Book: Crystal Structures.

[21] M. S. Bahramy, R. Arita and N. Nagaosa. Origin of giant bulk Rashba splitting: Application to BiTeI. *Phys. Rev. B*, vol. 84, 2011.

[22] K. Ishizaka, M. S. Bahramy, H. Murakawa, T. Shimojima, T. Sonobe, K. Koizumi, S. Shin, H. Miyahara, A. Kimura, K. Miyamoto, T. Okuda, H. Namatame, M. Taniguchi, R. Arita, N. Nagaosa, K. Kobayashi, Y. Murakami, R. Kumai, Y. Kaneko, Y. Onose and Y. Tokura. Giant Rashba-type spin splitting in bulk BiTeI. *Nature Mat.*, vol. 10, 2011.

[23] A. Crepaldi. *Strong spin-orbit coupling in low dimensional systems investigated by static and time-resolved ARPES*. PhD thesis, École Polytechinque Fédérale de Lausanne, 2012.

[24] P. D. C. King, T. D. Veal and C. F. McConville. Nonparabolic coupled Poisson-Schrodinger solutions for quantized electron accumulation layers: Band bending, charge profile, and subbands at InN surface. *Phys. Rev. B*, vol. 77, 2008.

[25] A. Crepaldi, L. Moreschini, G. Autés, C. Tournier-Colletta, S. Moser, N. Virk, H. Berger, Ph. Bugnon, Y. J. Chang, K. Kern, A. Bostwick, E. Rotenberg, O. V. Yazyev, M. Grioni. Giant Ambipolar Rashba Effect in the Semiconductor BiTeI. *Phy. Rev. Lett.*, vol. 109, 2012.

[26] M. Sakano, M. S. Bahramy, A. Katayama, T. Shimojima, H. Murakawa, Y. Kaneko, W. Malaeb, S. Shin, K. Ono, H. Kumigashira, R. Arita, N. Nagaosa, H. Y. Hwang, Y. Tokura and K. Ishizaka. Strongly Spin-Orbit Coupled Two-Dimensional Electron Gas Emerging near the Surface of Polar Semiconductors. *Phy. Rev. Lett.*, vol. 110, 2013.

[27] A. Damascelli, Z. Hussain and Z.-X. Shen. Angle-resolved photoemission studies on cuprate superconductors. *Rev. Mod. Phy.*, vol. 75, 2003.

[28] S. Hufner. *Photoemission Spectroscopy: Principles and Applications.* Springer-Verlag, 1995.

[29] S.K. Sundaram and E, Mazur. Inducing and probing non-thermal transitions in semiconductors using femtosecond laser pulse. *Nature Mat.*, vol. 1, 2022.

[30] Y. H. Wang, D. Hsieh, E. J. Sie, H. Steinberg, D. R. Gardner, Y. S. Lee, P. Jarillo-Herrero and N. Gedik. Measurement of Intrinsic Dirac Fermion Cooling on the Surface of the Topological Insulator Bi_2Se_3 Using Time-Resolved and Angle-Resolved Photoemission Spectroscopy. *Phys. Rev. Lett.*, vol. 109, 2012.

[31] J. A. Sobota, S. Yang, J. G. Analytis, Y. L. Chen, I. R. Fisher, P. S. Kirchmann and Z.-X. Shen. Ultrafast Optical Excitation of a Persistent Surface-State Population in the Topological Insulator Bi2Se3. *Phy. Rev. Lett.*, vol. 108, 2012.

[32] M. Hajlaoui, E. Papalazarou, J. Mauchain, G. Lantz, N. Moisan, D. Boschetto, Z. Jiang, I. Miotktowski, Y. P. Chen, A. Taleb-Ibrahimi, A. Taleb-Ibrahimi, L. Perfetti and M. Marsi. Ultrafast Surface Carrier Dynamics in the Topological Insulator Bi2Te3. *Nano Lett.*, vol. 12, 2012.

[33] A. Crepaldi, B. Ressel, F. Cilento, M. Zacchigna, C. Grazioli, H. Berger, Ph. Bugnon, K. Kern, M. Grioni and F. Parmigiani. Ultrafast photodoping and effective Fermi-Dirac distribution of the Dirac particles in Bi_2Se_3. *Phys. Rev. Lett.*, vol. 86, 2012.

[34] J. C. Johannsen, S. Ulstrup, F. Cilento, A. Crepaldi, M. Zacchigna, C. Cacho, I. C. E. Turcu, E. Springate, F. Fromm, C. Raidel, T. Seyller, F. Parmigiani, M. Grioni and P. Hofmann. Direct view on the ultrafast carrier dynamics in graphene. *arXiv*, 1304.2615, 2013.

[35] S. I. Anisimov, B. L. Kapeliovich, and T. L. Perelman. Electron emission from metal surfaces exposed to ultrashort laser pulses. *Eksp. Teor. Fiz.*, 1974.

[36] P. B. Allen. Theroy of relaxation of electrons in metals. *Phy. Rev. Lett.*, vol. 59, 1987.

[37] N. W. Aschroft and N. D. Mermin. *Solid state physics.* Harcourt College Publishers, 1976.

[38] N. Singhi. Two-Temperatures Model of non-equilibrium electron relaxation: A Review. *Int. J. Mod. Phys. B*, 24, 2010.

[39] I. Yu. Sklyadneva, R. Heid, K.-P. Bohmen, V. Chis, V. A. Volodin, K. A. Kokh, O. E. Tereshchenko, P. M. Echenique and E. V. Chulkov. Lattice dynamics of bismuth tellurohalides. *Phys. Rev. B*, vol. 86, 2012.

[40] F. Cilento. *Non-equilibrium phase diagram of $Bi_2Sr_2Y_{0.08}Cu_2O_{8+\delta}$ cuprate superconductors revealed by ultrafast optical spectroscopy* . PhD thesis, Universitá degli Studi di Trieste - Scuola di Dottorato in Fisica, 2011.

[41] X. Zhu, C. Howard, J. Guo and M. El-Batanouny. Electron-Phonon Coupling on the Surface of Topological Insulators. *arXiv*, 1307.4559, 2013.

[42] S. R. Park, J. Han, C. Kim, Y. Y. Koh, C. Kim, H. Lee, H. J. Choi, J. H. Han, K. D. Lee, N. J. Hur, M. Arita, K. Shimada, H. Namatame and M. Taniguchi. Chiral Orbital-Angular Momentum in the Surface States of Bi_2Se_3. *Phys. Rev. Lett.*, vol. 108, 2012.

[43] Y. H. Wang, D. Hsieh, D. Pilon, L. Fu, D. R. Gardner, Y. S. Lee and N. Gedik. Observation of a Warped Helical Spin Texture in Bi_2Se_3 from Circular Dichroism Angle-Resolved Photoemission Spectroscopy. *Phys. Rev. Lett.*, vol. 107, 2011.

[44] W. Jung, Y. Kim, B. Kim, Y. Koh, C. Kim, M. Matsunami, S. Kimura, M. Arita, K. Shimada, J. H. Han J. Kim, B. Cho, C. Kim. Warping effects in the band and angular-momentum structures of the topological insulator Bi_2Te_3. *Phys. Rev. Lett.*, vol. 84, 2011.

[45] G. Bian, L. Zhang, Y. Liu, T. Miller and T.-C. Chiang. Illuminating the Surface Spin Texture of the Giant-Rashba Quantum-Well System Bi/Ag(111) by Circularly Polarized Photoemission. *Phys. Rev. Lett.*, vol. 108, 2012.

[46] B. Kim, C. H. Kim, P. Kim, W. Jung, Y. Kim, Y. Koh, M. Arita, K. Shimada, H. Namatame, M. Taniguchi, J. Yu and C. Kim. Spin and orbital angular momentum structure of Cu(111) and Au(111) surface states. *Phys. Rev. B*, vol. 85, 2012.

[47] J.H. Park, C. H. Kim, J. W. Rhim and J. H. Han. Detecting Chiral Orbital Angular Momentum by Circular Dichroism ARPES. *arXiv:1112.1821v1.*, 2011.

[48] M. R. Scholz, J. Sánchez-Barriga, J. Braun, D. Marchenko, A. Varykhalov, M. Lindross, Y. J. Wang, H. Lin, A.Bansil, J. Minar, H. Ebert, A. Volykhov, L. V. Yashina and O. Rader. Reversal of the Circular Dichroism in Angle-Resolved Photoemission from Bi_2Te_3. *Phy. Rev. Lett.*, vol. 110, 2013.

[49] D. Hsieh, Y. Xia, D. Qian, L. Wray, J. H. Dil, F. Meier, J. Osterwalder, L. Patthey, J. G. Checkelsky, N. P. Ong, A. V. Fedorov, H. Lin, A. Bansil, D. Grauer, Y. S. Hor, R. J. Cava and M. Z. Hasan. A tunable topological insulator in the spin helical Dirac transport regime. *Nature*, vol. 460, 2009.

[50] Z.-H. Pan, E. Vescovo, A. V. Fedorov, D. Gardner, Y. S. Lee, S. Chu, G. D. Gu and T. Valla. Electronic Structure of the Topological Insulator Bi_2Se_3 Using Angle-Resolved Photoemission Spectroscopy: Evidence for a Nearly Full Surface Spin Polarization. *Phy. Rev. Lett.*, vol. 106, 2011.

[51] C. Jozwiak, Y. L. Chen, A. V. Fedorov, J. G. Analytis, C. R. Rotundu, A. K. Schmid, J. D. Denlinger, Y.-D. Chuang, D.-H. Lee, I. R. Fisher, R. J. Birgeneau, Z.-X. Shen, Z. Hussain and A. Lanzara. Widespread spin polarization effects in photoemission from topological insulators. *Phy. Rev. B*, vol. 84, 2011.

[52] Z.-H. Zhu, C. N. Veenstra, G. Levy, A. Ubaldini, P. Syers, N. P. Butch, J. Paglione, M. W. Haverkort, I. S. Elfimov and A. Damascelli. Layer-by-Layer entagled spin-orbital texture of the topological surface stase in Bi_2Se_3. *Phy. Rev. Lett.*, vol. 110, 2013.

[53] J. Premper, M. Trautmann, J. Henk and P. Bruno. Spin-orbit splitting in an anisotropic two-dimensional electron gas. *Phys. Rev. B*, vol. 76, 2007.

Ringraziamenti

Prima di tutti devo ringraziare Alberto e Federico, che pazientemente mi hanno guidato in tutto il lavoro, insegnandomi e facendomi appassionare a questo progetto. Grazie per il legame di amicizia vissuto in questi mesi che va oltre il semplice lavoro in laboratorio: senza di voi questa tesi non sarebbe stata la stessa. E grazie a Michele, fonte di qualsiasi informazione possibile su Trieste, per l'aiuto e la simpatia ricevuti in questi mesi.

Un enorme ringraziamento va al Prof. Parmigiani, per aver reso tutto questo possibile seguendo con premura ogni passo del lavoro, per i suoi fondamentali consigli, non solo nel campo della fisica, e per il suo modo unico di leggere ogni situazione e ogni persona assicurandosi che "il fuoco della fisica" non si estingua.

A tutte le persone del T-ReX, per il bellissimo gruppo che hanno creato, per le svariate conversazioni e tutto il tempo passato insieme.

Cicerone scriveva: "L'amicizia comporta moltissimi vantaggi. Dovunque tu vada è a tua disposizione, non è esclusa da nessun luogo, non è mai inopportuna, non è mai un peso." Per me è così, e in questo mio percorso di cinque anni nell'estremo oriente d'Italia gli amici sono stati una presenza costante e fondamentale ed a tutti loro va un immenso grazie.

In particolare a Marta, la migliore compagna di banco possibile, per le lunghe giornate e nottate passate assieme a preparare gli esami, per alcune serate indimenticabili e per i thè pomeridiani a cornice delle innumerevoli conversazioni avute in questi anni.

A Zambo, per le infinite ore trascorse insieme ad analizzare i dati per la relazione di laboratorio e per la grandiosa compagnia, oltre all'intramontabile grido "Al Nord!", con cui ha impreziosito i nostri viaggi nell'Europa settentrionale, anche se resta un mistero come siamo riusciti a tornare vivi dalle innevate lande scozzesi senza fare nemmeno un graffio alla macchina presa a noleggio.

A Erik, che ha sempre avuto la battuta pronta per ogni situazione e che è stato una sicurezza per le immancabili birrette insieme del dopo-cena o durante le partite.

A Franz, con cui il rapporto di amicizia dura da quel famoso giorno di settembre di cinque anni fa in cui, giovani matricole, ci conoscemmo dopo lo scritto della Fonda. Da quel giorno la nostra amicizia si è consolidata, supportata dalla condivisione della preparazione di alcuni esami, dalla vita da vicini di casa e soprattutto dall'istinto che ci ha spinto ad affidarci al Prof. Parmigiani per lo svolgimento delle nostre tesi e che si è poi rivelata la scelta migliore che potes-

simo fare.

A Francesca, la cui casa è per me sempre stata aperta a chiaccherate di gioie e pettegolezzi e per il suo prezioso aiuto e sostegno in un momento di sbandamento; a Barbara, con cui ho avuto la fortuna di condividere senza ripensamenti l'idea un po' folle di un viaggio quasi improvvisato nella calda terra siciliana, rivelatosi poi una vacanza straordinaria.

A Giulio, inimitabile e insostituibile per la sua capacità unica di trasformarsi istantaneamente nella star delle serate, compresa l'ultima grande notte di delirio a Copenhagen; ai DJ "made in Friuli" ufficiali e affidabili del nostro gruppo a cui dobbiamo la buona riuscita di tante feste organizzate in questi anni: il Turcaz, con la sua pacatezza e il geniale umorismo e Davide, folle genio friuliano ormai trapiantato a Parigi, che ha tracciato la strada percorsa tra le brughiere scozzesi.

Al Guazzo, per il sorriso con cui mi ha sempre risposto alle innumerevoli volte in cui gli ho chiesto in prestito l'auto e per la sua ostinazione a sostenere la supremazia della fisica computazionale ben sapendo di avere torto; a Luca, senza il quale le partite del JH non sarebbe assolutamente state le stesse.

Alle ragazze "acquisite" del gruppo diventate in poco tempo parte irrinunciabile della compagnia: Silvia, per la sua esuberanza contagiante e la sua tenerezza; Stefania, non solo per averci restituito l'Erik migliore, ma soprattutto per l'ondata di allegria che riesce sempre a portare in mezzo a noi; Cate, per il tentativo di separare gli inseparabili Zamborlini e Giulio e per non aver rinunciato a far parte di questo pazzo gruppo di fisici.

Un posto particolare nella mia vita degli ultimi due anni lo occupa il mio coinquilino Stefano. Grazie, perchè le conversazioni di ore su argomenti particolari, così poco di moda tra i giovani d'oggi ma così importanti, la pacatezza e la fiducia con cui affronti la vita e il modo unico con cui vedi il mondo, cercando di non scendere mai al livello dei rapidi e facili giudizi, mi hanno donato quella serenità e quella pace che permettono di chiamare un appartamento, con le persone che ci vivono, semplicemente e sinceramente "casa".

A coloro che, dopo una sola settimana dal nostro primo arrivo e incontro a Trieste, diventarono subito come amici di vecchia data: Salvo, Manuel e Michele, la prima vera e unica Accademia, e Enea, per la solarità e la spontaneità della loro amicizia fin dal primo momento, per la loro positiva imprevedibilità e capacità di sorprendermi e per avermi dato la spinta e la possibilità di inziare a scoprire la bellezza incantevole del Sud Italia.

Grazie a tutti voi per lo splendido gruppo che abbiamo creato, mai avrei potuto immaginare di trovarne uno così bello.

A Enrico, che si è dimostrato una persona sempre disponibile e che mi ha permesso di vedere tante situazioni con un'ottica diversa; to Sani, for her ever present smile and for the opportunity she gave me to get to know the Nepalese culture.

Ai miei primi coinquilini Elisa e Alberto diventati buoni amici con cui condividere un ottimo mojito fatto in casa nel bel mezzo della notte e per avermi fatto sentire a casa in una città totalmente nuova.

A tutti voi, e a tutti coloro con cui ho condiviso momenti unici di questi

cinque anni, un profondo e sincero grazie.

Un mio grazie è rivolto inevitabilmente ai miei legami veronesi, che anche a trecento chilometri di distanza mi hanno dato una spinta importante. Tra questi ricordo con affetto la mia professoressa Fiorella per aver incoraggiato e alimentato negli anni di Liceo il seme della passione per la fisica che ha intravisto in me poco dopo il nostro primo incontro, e Isabelle per avermi insegnato ad ascoltare davvero la musica, a cercarla dentro di me e ad usarla come spinta per migliorarmi costantemente.

Un grazie particolare ad Alessandro, che ha compiuto il mio stesso percorso tra le montagne del trentino, continuando a condividere fatti, momenti ed impressioni dei nostri cammini e sostenendoci a vicenda nelle situazioni cruciali della nostra scalata parallela al "monte della fisica".

A Francesco alias Aliuccio, per gli innumerevoli momenti passati insieme, per le conversazioni di ore, per i suoi consigli preziosi e per tutto quello che abbiamo condiviso, di una richezza che va aldilà di quanto qualsiasi parola potrai mai descrivere. Ma più di tutto, grazie per l'inestimabile semplicità con cui ci siamo sempre ritrovati dopo che i tempi e le distanze delle rispettive vite ci avevano tenuti separati. A te va il mio ringrazimento speciale per essere molto di più di un semplice quasi cognato.

Ai miei zii e cugini, perchè con loro sono cresciuta e ai miei nonni, che riposano nel mio cuore, per avermi insegnato come anche i gesti e le parole più semplici possono essere nella vita tesori preziosi e suscitare ricordi bellissimi.

Un grazie inestimabile a mio fratello Paolo e a mia sorella Irene, veri pilastri della mia vita e senza i quali assolutamente nulla sarebbe lo stesso. Grazie, perchè indipendentemente dai vari impegni, dalla distanza che ci separa e dalle differenze che ci contraddistinguono vi ho sempre trovato pronti a darmi il vostro sostegno, il vostro conforto, i vostri consigli. Grazie, perchè l'assoluta certezza di avervi accanto mi ha dato la forza e il coraggio di superare anche i momenti più duri e le difficoltà che parevano insormantabili.

E un grazie più grande di immenso e aldilà di infinito ai miei genitori che più di tutti hanno e continuano a credere in me, sempre e comunque. Tante parole davvero non bastano per esprimere quanto è profondo il mio grazie per voi che riuscite sempre a farmi sentire come se potessi sfiorare il cielo con un dito. Questo traguardo è anche vostro.